Computation of Recirculating Swirling Flow with the GLM Reynolds Stress Closure

by

Song Fu and S.B. Pope

FDA 93-06 March 1993

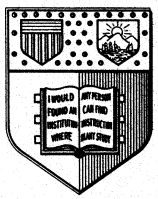

Fluid Dynamics and Aerodynamics Program

Sibley School of
Mechanical and Aerospace Engineering

Cornell University Ithaca, New York 14853

Computation of Recirculating Swirling Flow with the GLM Reynolds Stress Closure

Song Fu
Department of Engineering Mechanics
Tsinghua University
Beijing 100084, China

and

S.B. Pope
Sibley School of Mechanical and Aerospace Engineering
Cornell University
Ithaca, NY 14853

Abstract

A Reynolds stress closure based on the generalized Langevin model (GLM), developed by Haworth and Pope [3, 4] (from a general equation for describing the fluid particle velocity increment in the probability density function method), is applied to the flow calculation with swirl-induced recirculation. The purpose of the work is to assess the performance of this model under the complex flow conditions caused by the presence of strong swirl which gives rise to both unconventional recirculation in the vicinity of the symmetry axis and strong anisotropy in the turbulence field. Comparison of the computation results are made both with the experimental data of Roback and Johnson [11] and the computational results obtained with the typical isotropization of production model (IPM) and the $k - \epsilon$ type Boussinesq viscosity model.

1 Introduction

Modelling of turbulent flows has followed a traditional path pioneered by Osborn Reynolds that the turbulent quantities are decomposed into mean and fluctuating parts. The mean flow equations can be obtained by averaging the governing equations, the Navier-Stokes equations, and the correlations of the fluctuating velocity components resulting from the averaging process, the Reynolds stresses, then contain the turbulence statistics. The Reynolds stresses are unknown quantities in the mean flow equations. Their magnitudes have a critical influence over the solution of the entire flow field, and therefore these Reynolds stresses need to be modelled appropriately. Current modelling strategies fall basically into two types: Boussinesq eddy viscosity hypothesis and second-moment closures. These two approaches in the turbulence modelling research field have received a great deal of attention in the last two decades, but the application of the subsequent models gives sometime satisfactory and sometimes less encouraging results. The main failure of the computations lies in the area of complex flow fields where either or both strong anisotropy in turbulence properties and flow recirculation occurs. Strongly swirling flow with recirculation is such a typical example that the current models have yet to produce satisfactory computational results both in terms of mean flow and turbulence quantities, although the second-moment closures have demonstrated superiority over the Boussinesq viscosity models in many applications [6, 8, 9].

Alternatively, an evolution equation for the joint probability density function (pdf) of the velocities, as well as scalars, can be derived and modelled to describe turbulence activities. This approach offers several advantages: the joint pdf contains more statistical information than is contained in a finite number of moments and some of the terms that must be modelled in the moment closure methods appear in closed form in the pdf evolution equation. The essence of this modelling strategy is to adopt the Lagrangian viewpoint of turbulence that the history of the fluid particles in turbulent flows provides a complete description of the turbulence. Indeed, following the generalization of the Langevin equation proposed by Pope [1] to model the Lagrangian velocity increment, Haworth and Pope [3] were able to derive a different type of Reynolds-stress evolution equation. They were also able to close this equation through modelling and calibrate the subsequent model against a broad range of experiments. It was observed that the GLM

type Reynolds stress closure exhibited satisfactory performance in the homogeneous shear flow calculations [3], and later re-optimization of the model also led the computational results to reasonably good agreement with experiments in free shear flows [4]. These encouraging applications of the GLM in simple flow calculations provide strong incentives to its application in the complex flow case. Thus, the present work focuses on the performance of the GLM in the complex flow, in particular, in the strongly swirling recirculating flow of Roback and Johnson [11].

2 Mathematical Description of the Flowfield

2.1 Lagrangian Description

In the Lagrangian viewpoint, the flow properties are revealed by describing the history of the fluid particles. By definition, the rate of change of a fluid particle's position is its velocity: the velocity must change in accordance with the Navier-Stoke equation. In an increment of time dt, the increments in fluid particle position and velocity are given by [2]

$$dx_i^+ = U_i^+ dt, \tag{1}$$

$$dU_i^+ = -\frac{1}{\rho}\frac{\partial P}{\partial x_i}dt + \left(\nu\nabla^2 u_i - \frac{1}{\rho}\frac{\partial p}{\partial x_i}\right)dt, \tag{2}$$

where, x_i^+ and U_i^+ denote the components of the fluid particle position and velocity in the i-direction, respectively, at time t. In these equations, the Eulerian velocity and pressure fields have been decomposed into their means $U(\mathbf{x},t)$ and $P(\mathbf{x},t)$ and the fluctuations $u(\mathbf{x},t)$ and $p(\mathbf{x},t)$. These Eulerian quantities are evaluated at the particle position $\mathbf{x}(t)$. The fluid properties are the density ρ and the kinematic viscosity ν, all assumed to be constant in the present analysis. The term $\nu\nabla^2 U_i$ has been omitted as only high Reynolds number turbulent flows are considered here.

2.2 Generalized Langevin Equation

According to the generalized Langevin model for equation (2), the increment in particle velocity $\mathbf{U}^*(t)$ in a time interval dt is given by

$$dU_i^* = -\frac{1}{\rho}\frac{\partial P}{\partial x_i}dt + G_{ij}(U_j^* - U_j)dt + (C_0\epsilon)^{1/2}dW_i(t), \tag{3}$$

i.e., the particle velocity is governed by a stochastic differential equation of the Langevin type. The notation * is used to distinguish this modelled particle from a fluid particle. The term $G_{ij}(\mathbf{x}, t)$ in equation (3) is a function of the one-point pdf, i.e., a function of one-point dynamic field, C_0 is a universal constant, ϵ represents the mean dissipation rate of turbulent kinetic energy, and $\mathbf{W}(t)$ denotes an isotropic Wiener process. This process is Markovian and stochastic in nature with increments $d\mathbf{W}(t) = \mathbf{W}(t+dt) - \mathbf{W}(t)$ having a joint-normal distribution of zero means and an isotropic covariance matrix,

$$< dW_i(t) >= 0, \qquad < dW_i(t)dW_j(t) >= \delta_{ij}dt, \tag{4}$$

where the angled brackets represent the expectation of the stochastic processes inside.

Equation (3) represents a linear Markov model for the fluid particle velocity, analogous to the Langevin equation for the velocity of a particle undergoing Brownian motion. The justification for the inclusion of the stochastic term can be proved from its consistency with Kolmogorov's inertial range scaling laws [3]. The basic assumptions embodied in the generalized Langevin equation (3) are that the Markovian stochastic process $\mathbf{W}(t)$ and the $G_{ij}(t)$ terms represent local mean flow quantities, implying that the model applies only to those flows where turbulence structures can be expressed in terms of local mean quantities; and that the inertial range scales are locally isotropic.

Equation (3) also forms a basis where the connection between the Langevin equation and the Reynolds-stress evolution equation can be established. It can be shown that through the evolution equation for the joint pdf of the velocities corresponding to the Langevin model, a modelled Reynolds-stress transport equation can also be derived which reads:

$$\frac{D\overline{u_iu_j}}{Dt} = -\frac{\partial\overline{u_iu_ju_k}}{\partial x_k} + P_{ij} + G_{ik}\overline{u_ku_j} + G_{jk}\overline{u_ku_i} + C_0\epsilon\delta_{ij}, \tag{5}$$

where,

$$P_{ij} = -\overline{u_i u_k}\frac{\partial U_j}{\partial x_k} - \overline{u_k u_j}\frac{\partial U_i}{\partial x_k}.$$

Corresponding to the exact transport equation of the Reynolds stresses obtained from the Navier-Stokes equations [7], it is not difficult to show that the last three terms in the above equation represent the pressure and viscous correlations in the second-moment closures, i.e.,

$$\begin{aligned} &G_{ik}\overline{u_k u_j} + G_{jk}\overline{u_k u_i} + C_0\epsilon\delta_{ij} = \\ &\quad -\frac{1}{\rho}\left(\overline{u_j\frac{\partial p}{\partial x_i}} + \overline{u_i\frac{\partial p}{\partial x_j}}\right) + \nu(\overline{u_i\nabla^2 u_j} + \overline{u_j\nabla^2 u_i}). \end{aligned} \tag{6}$$

This compatibility between the Langevin model and second-order models is a direct consequence of the linearity of the deterministic term in the velocity components in equation (3).

2.3 Closure of G_{ij} Terms

Haworth and Pope [3] proposed a functional form for G_{ij} that is linear in the mean velocity gradients and Reynolds stresses. The form is:

$$G_{ij} = \frac{\epsilon}{k}(\alpha_1\delta_{ij} + \alpha_2 b_{ij}) + H_{ijkl}\frac{\partial U_k}{\partial x_l}, \tag{7}$$

where

$$\begin{aligned} H_{ijkl} \;=\; &\beta_1\delta_{ij}\delta_{kl} + \beta_2\delta_{ik}\delta_{jl} + \beta_3\delta_{il}\delta_{kj} + \gamma_1\delta_{ij}b_{kl} + \gamma_2\delta_{ik}b_{jl} + \\ &\gamma_3\delta_{il}b_{jk} + \gamma_4\delta_{kl}b_{ij} + \gamma_5\delta_{lj}b_{ki} + \gamma_6\delta_{kj}b_{il}. \end{aligned}$$

Here, b_{ij} is the normalized Reynolds-stress anisotropy tensor defined by $b_{ij} = \overline{u_i u_j}/\overline{u_k u_k} - \frac{1}{3}\delta_{ij}$. The expression (7) contains 11 coefficients, of which 7 can be deduced from the Navier-Stokes equation, and the remaining 4 are determined by experimental data [3]. The values of these coefficients are listed in the following table.

Generalized Langevin Model Coefficients

α_2	β_1	β_2	β_3	γ_1	γ_2	γ_3	γ_4	γ_5	γ_6
3.78	−0.2	0.8	−0.2	−1.24	1.04	−0.34	0	1.99	−0.76

The coefficient α_1 is determined through the contraction of equation (5) such that it becomes the transport equation of the turbulence kinetic energy, and the constraint on α_1 is then,

$$\alpha_1 = -\left(\frac{1}{2} + \frac{3}{4}C_0\right) - \alpha_2 b_{ii}^2 - \frac{k}{\epsilon}[(\beta_2 + \beta_3 + \gamma^*/3)I_1 + \gamma^* I_2] \tag{8}$$

with $C_0 = 2.1$, $b_{ii}^2 = b_{il}b_{li}$, $\gamma^* = \gamma_2 + \gamma_3 + \gamma_5 + \gamma_6$ and

$$I_1 = b_{ij}\frac{\partial U_i}{\partial x_j}, \qquad I_2 = b_{ik}b_{kj}\frac{\partial U_i}{\partial x_j}. \tag{9}$$

With expression (7), a closed form of the Reynolds-stress evolution equation can be obtained from equation (5) by substituting the former into the latter. But before doing this, it is helpful to notice that the expression (6) indicates that the G_{ij} terms physically account for the interactions between fluctuating velocities and pressure gradients. It can be shown easily that these pressure terms can be decomposed into two parts: one provides the mechanism of transferring turbulence energy among its components, the other corresponds to the diffusion transport due to pressure fluctuation. In the evolution process, it is observed that away from the solid wall, the diffusion terms play only a secondary role in the overall balance of the Reynolds stresses. It is therefore plausible to attribute the G_{ij} terms to be primarily responsible for the energy redistribution. Thus, expression (6) can be rewritten as

$$G_{ik}\overline{u_k u_j} + G_{jk}\overline{u_k u_i} + C_0\epsilon\delta_{ij} = \phi_{ij} - \frac{2}{3}\delta_{ij}\epsilon. \tag{10}$$

The ϕ_{ij} term, then, represents the redistribution process with zero trace on contraction, and hence can be written in an isotropization form which can be deduced by substituting the G_{ij} model into the above expression. That is:

$$\begin{aligned}
\phi_{ij} \;=\; & 4\epsilon\left[\left(\alpha_1 + \frac{1}{3}\alpha_2\right)b_{ij} + \alpha_2\left(b_{ij}^2 - \frac{1}{3}\delta_{ij}b_{kk}^2\right)\right] + \\
& 2k\left[\gamma_2\left(E_{ij} - \frac{2}{3}\delta_{ij}I_2\right) + \gamma_3\left(F_{ij} - \frac{2}{3}\delta_{ij}I_2\right) + (\gamma_5 + \gamma_6)\left(M_{ij} - \frac{2}{3}\delta_{ij}I_2\right)\right] \\
& -\lambda_1\left(P_{ij} - \frac{1}{3}\delta_{ij}P_{kk}\right) - \lambda_2\left(D_{ij} - \frac{1}{3}\delta_{ij}P_{kk}\right) - \frac{2}{9}\gamma^* k S_{ij},
\end{aligned} \tag{11}$$

where,

$$D_{ij} = -\overline{u_i u_k}\frac{\partial U_k}{\partial x_j} - \overline{u_k u_j}\frac{\partial U_k}{\partial x_i}, \qquad S_{ij} = \frac{\partial U_i}{\partial x_j} + \frac{\partial U_j}{\partial x_i},$$
$$E_{ij} = b_{ik}^2\frac{\partial U_j}{\partial x_k} + b_{jk}^2\frac{\partial U_i}{\partial x_k}, \qquad M_{ij} = b_{ik}b_{jl}S_{kl},$$
$$F_{ij} = b_{ik}^2\frac{\partial U_k}{\partial x_j} + b_{jk}^2\frac{\partial U_k}{\partial x_i}, \qquad b_{ij}^2 = b_{il}b_{lj};$$

and, $\lambda_1 = \beta_2 + (\gamma_2 + \gamma_6)/3$, $\lambda_2 = \beta_3 + (\gamma_3 + \gamma_5)/3$. It may be observed that the redistribution model ϕ_{ij} formulated in equation (11) does not contain the coefficients β_1 and γ_1 even though they are active in the Langevin equation. This indicates that some turbulence statistical information contained in the pdf solution are lost in the G_{ij} model.

The redistribution model displayed by equation (11) has some interesting properties. The model is nonlinear in the anisotropy tensor of the Reynolds stresses b_{ij}. The terms on the first line on the right-hand side represent a nonlinear return-to-isotropy process. This nonlinearity is found necessary even in the turbulence decay process [10]. The second line represents the interactions between the quadratic anisotropy tensor with the mean velocity gradients, a process that has now been widely accepted [6, 12]. The terms on the third line have identical form to the Launder, Reece and Rodi's Quasi-Isotropization Model (QIM). In fact, the expression (11) may be viewed as a nonlinear extension of QIM with quadratic terms in the Reynolds-stress anisotropy tensor b_{ij} added on. However, this resemblance is not complete since the strain rate S_{ij} related redistribution process totally depends on the nonlinear extensions in the GLM. The absence of these quadratic terms diminishes the presence of the strain-rate-related terms which stand alone in the QIM. Also, the expression (11) can easily be reverted to Rotta and the Isotropization of Production Model (IPM) by setting all the coefficients in this expression to zero apart from α_1 and λ_1. In this way, it becomes

$$\phi_{ij} = -c_1\epsilon b_{ij} - c_2\left(P_{ij} - \frac{1}{3}\delta_{ij}P_{kk}\right), \tag{12}$$

with $c_1 = -4\alpha_1 = (2 + 3C_0) - 2\beta_2 P/\epsilon$ and $c_2 = \lambda_1 = \beta_2$. However, C_0 has to be a function of the ratio of the energy production over its dissipation rate,

P/ϵ, for c_1 to take the widely accepted constant 3.6. In fact, in this case,

$$C_0 = \frac{1}{3}\left(c_1 - 2 + 2\beta_2\frac{P}{\epsilon}\right).$$

To complete the Reynolds-stress model, the triple velocity correlation $\overline{u_i u_j u_k}$ is modelled by the Daly and Harlow's gradient type model [5] which gives:

$$-\overline{u_i u_j u_k} = c_s\frac{k}{\epsilon}\overline{u_k u_l}\frac{\partial \overline{u_i u_j}}{\partial x_l}, \tag{13}$$

with $c_s = 0.22$.

2.4 Remaining Equations for the Solution

The above analysis leads to the closure of the second-moment equations derived from the generalized Langevin model. The complete solution of the flowfield requires the solutions of the momentum and continuity equations which have the following Cartesian tensor forms:

Momentum

$$U_j\frac{\partial U_i}{\partial x_j} = -\frac{1}{\rho}\frac{\partial P}{\partial x_i} + \frac{\partial}{\partial x_j}\left[\nu\left(\frac{\partial U_i}{\partial x_j} + \frac{\partial U_j}{\partial x_i}\right) - \overline{u_i u_j}\right]. \tag{14}$$

Continuity

$$\frac{\partial U_i}{\partial x_i} = 0. \tag{15}$$

It is clear from equation (14) that the mean flow variables are strongly coupled with the Reynolds stresses. In the solution procedure, all three velocity and six Reynolds stress components have to be solved in the present case of swirling flow, although the flow is axisymmetric. To complete the closure of the problem, the dissipation rate of the turbulence kinetic energy is obtained through the following equation:

$$U_j\frac{\partial \epsilon}{\partial x_j} = \frac{\partial}{\partial x_k}\left(c_\epsilon\frac{k}{\epsilon}\overline{u_k u_l}\frac{\partial \epsilon}{\partial x_l}\right) + \frac{\epsilon}{k}(C_{\epsilon 1}\frac{1}{2}P_{kk} - C_{\epsilon 2}\epsilon) \tag{16}$$

The coefficients c_ϵ, $C_{\epsilon 1}$ and $C_{\epsilon 2}$ retain their standard values, 0.18, 1.45 and 1.92, respectively.

2.5 $k-\epsilon$ Two-equation Model

In the $k-\epsilon$ model the Reynolds stresses assume the validity of the Boussinesq hypothesis that the anisotropy of the Reynolds stresses are linearly proportional to the mean strain rate:

$$-\overline{u_i u_j} = \nu_t \left(\frac{\partial U_i}{\partial x_j} + \frac{\partial U_j}{\partial x_i} \right) - \frac{2}{3}\delta_{ij}k, \tag{17}$$

where $k = \overline{u_i u_i}/2$ is the turbulent kinetic energy, ν_t is the isotropic turbulent eddy viscosity defined in the context of $k-\epsilon$ model as $\nu_t = C_\mu k^2/\epsilon$.

The turbulent kinetic energy k and the dissipation rate ϵ are governed by their modelled transport equations:

$$U_j \frac{\partial k}{\partial x_j} = \frac{\partial}{\partial x_j} \left[\left(\nu + \frac{\nu_t}{\sigma_k} \right) \frac{\partial k}{\partial x_j} \right] + P - \epsilon, \tag{18}$$

and

$$U_j \frac{\partial \epsilon}{\partial x_j} = \frac{\partial}{\partial x_j} \left[\left(\nu + \frac{\nu_t}{\sigma_\epsilon} \right) \frac{\partial \epsilon}{\partial x_j} \right] + \frac{\epsilon}{k}(C_{\epsilon 1} P - C_{\epsilon 2}\epsilon), \tag{19}$$

where $P = 0.5\nu_t(\partial U_i/\partial x_j + \partial U_j/\partial x_i)^2$ contributes to a positive source term in the above equations, representing the turbulence production. The values of the coefficients in the above equations are: $C_\mu = 0.09$, $\sigma_k = 1.0$ and $\sigma_\epsilon = 1.22$.

2.6 Numerical Solution

The model equations are solved numerically by a finite volume method employing the SIMPLE algorithm. A grid of 50×100 nodes is used, preliminary tests having shown that the solutions obtained are little different on a grid twice as large.

3 Results and Discussion

The strongly swirling flow of Roback and Johnson was chosen here to be the test case. The geometry of the flowfield consists of two coaxial jets through which the flow enters an axisymmetric chamber with sudden expansion. The inner and annular jets have diameters $0.025m$ and $0.049m$ respectively. The

diameter of the chamber is $0.122m$. The swirl velocity component is introduced to the chamber through the annular jet. It is observed in the experiment that the swirl strength is so strong that a central recirculation is formed in the vicinity of the axis of symmetry. The flow can be considered as isothermal and steady state.

3.1 Mean Flow Quantities

Figure 1 shows the streamfunction contour plots calculated with the $k-\epsilon$ model and with the IPM and GLM second-moment closures, respectively. It is seen that the first two give roughly the same length of the recirculation size in the vicinity of the symmetry axis, whereas the GLM produces a very elongated one extending right to the exit boundary. The flow patterns exhibited by all the three models differ significantly. The size of the central recirculation, induced by the strong-swirl inlet condition, can be best illustrated from the axial velocity development along the axis, as is shown in figure 2. There, it is seen that all the models fail to provide the velocity recovery indicated by the experiment after the recirculation. The GLM fails to recover the velocity even to the positive value suggesting a sustained reverse flow pattern near the axis. The GLM also exhibits a unrealistic recovery just before the reverse flow occurs. The cause of this behavior is believed to be the effect of the interaction of the annular and inner jet flows reaching the axis of symmetry. Compared with the experiment of Roback and Johnson [11], the size of the recirculation is well captured by the IPM, and the $k-\epsilon$ model performed reasonably well. The reverse flow occurs on the axis of symmetry in the range of $x = 0.04m - 0.17m$.

The pressure and angular velocity contours are given in figure 3 and 4, respectively. A distinct feature of the pressure contours is that the GLM shows very small pressure gradients near the axis of symmetry after recirculation has occurred, as the pressure contour lines become almost parallel with the axis there. But this is in accord with the large recirculation shown by the GLM. It may be explained that the elongated recirculation is due to the lack of large pressure gradients which cause the flow to recover. The angular velocity contours all show large values towards the axis. The $k-\epsilon$ model also exhibits a center of precession with the maximum point falls on the axis inside the recirculation zone, while the two second-moment closure models give rise to precessing tubes and the strength of the tube produced

with the GLM is profound, consistent, again, with the phenomenon of large recirculation in the GLM results.

Shown in figures 5 and 6 are profiles of the axial velocity, U, and the swirling velocity, W, at locations $x = 0.025m$, $0.051m$, $0.102m$, $0.152m$ and $0.203m$, respectively. As the flow enters the chamber, all models give good agreement with the experimental data, as seen in figure 5(a) and figure 6(a). This is due to the dominance of the inlet conditions on the near flowfield. Inside the recirculation zone, the models capture the basic features of the axial velocities, figure 5(b,c), with GLM producing somewhat unrealistic shape near the axis. At the end and the recovering region of the flowfield, the quality of both $k-\epsilon$ and the IPM are comparable, but the strange behavior of the GLM persists in the entire field (figure 5(d,e)). Looking at the swirling velocity inside and in the recovery region, none of the models can be claimed to be superior to the others (figure 6(b–e)). Again, GLM displayed particular behavior giving maximum W-velocity close to the axis. This may also be associated with the U-profiles of the GLM where unrealistic peaks occur.

Overall, the basic mean flow features have been captured by the IPM and the $k-\epsilon$ model but none of them is very satisfactory. The GLM behaves in a strange manner, this is likely due to the nonlinear effects in the redistribution process, as the nonlinear models need further investigation in general.

3.2 Turbulence Quantities

The differences in the above mean flow quantities are obviously caused by the different values of the Reynolds stresses with differing modelling strategy in the mean flow equations. The turbulence quantities predicted by these three models should provide the answer to the different behavior of the model performance.

The overall feature of the turbulence quantities can be seen from figures 7 and 8, respectively, where the contours of the turbulence kinetic energy and dissipation rate are given. A common feature there for all the model results is that the maximum turbulence kinetic energy and dissipation rate occur at the edges of the recirculation zones near the corner recirculation. This is because of the very large shear strains existed there due to the presence of the two recirculations. The GLM seems to produce less intense turbulence energy than the IPM, this partly explains why the central recirculation is so large for the GLM results, for smaller turbulence energy implies a smaller

turbulent diffusion coefficient.

The shear stresses $\overline{uv}$ and $\overline{vw}$ are shown in figure 9. It is seen that the all the model results have large errors relative to the experiment. In fact, the $k-\epsilon$ model may even be said to have performed better than the second-moment closure IPM. This shows that the Reynolds shear stress $\overline{uv}$ is strongly and linearly related to the mean strain rate in this flow. It can be observed that the GLM persistently underpredicts this shear stress throughout the whole flowfield. This is believed to be the prime cause for the occurrence of the excessive central recirculation exhibited by the GLM, since the shear stress $\overline{uv}$ is directly responsible for turbulence mixing. It is difficult to speculate, however, on which element in the redistribution equation of GLM, equation (11), causes this underprediction. One possible reason might be that the coefficients γ_2 and γ_3 have different signs which may not be appropriate. The terms associated with these two coefficients, E_{ij} and F_{ij}, can be seen as the nonlinear extension of the terms P_{ij} and D_{ij}, respectively. These latter two terms have the coefficients, λ_1 and λ_2, of the same sign.

The shear stress $\overline{vw}$ profiles are given in figure 10. Since no comparison can be made with the experiment, it is difficult to assess the performance of the models. But again, the GLM shows consistent behavior of underpredicting the magnitude of this shear stress as in the case for $\overline{uv}$. For the sake of reference, the anisotropy invariants maps (AIM) for both the GLM and IPM calculations are also presented in figure 11. It is seen here that both results satisfy the realizability condition as all points fall inside the triangular shaped enclosure whose vertical axis is $(b_{ii}^2)^{1/2}$ and the horizontal axis $(b_{ii}^3)^{1/3}$.

4 Conclusion

The present study investigated the performance of the second-moment closure derived from the probability-density function analysis. In particular, the Roback and Johnson strongly swirling flow was studied with the generalized Langevin model which was first designed for modelling the fluid particle velocity increment in the Lagrangian viewpoint of the fluid motion. An isotropization form of the GLM was derived which gives clear interpretation of the individual terms in this redistribution process. It is observed that the GLM can be seen as a nonlinear extension of the Rotta and Launder, Reece

and Rodi models. The GLM can also be easily contracted to the IPM.

The computation results show that the GLM produces excessive strength of the recirculation. The best agreement with the experiment on the size of the recirculation is obtained with the IPM. Looking at the mean flow and turbulence quantity profiles, none of the models appeared to have performed superior than the others, in fact, the $k-\epsilon$ model results were as good as that from the IPM. The GLM, however, generally underpredicts the Reynolds shear stresses, giving less turbulent mixing. This is believed to be prime cause of the elongated recirculation exhibited by the GLM. The reason for the unconventional velocity profiles by the GLM is unclear. The nature of the nonlinearity of the model requires further study.

References

[1] Pope S. B. *Phys. Fluids A*, 26:404, 1983.

[2] Pope S. B. *Prog. Energy. Comb. Sci.*, 11:119, 1985.

[3] Haworth D. C. and Pope S. B. A generalized langevin model for turbulent flows. *Phys. Fluids A*, 29(2):pp.387–405, 1986.

[4] Haworth D. C. and Pope S. B. A pdf modeling study of self-similar turbulent free shear flows. *Phys. Fluids A*, 30(4):pp.1026–1044, 1987.

[5] B. J. Daly and F. H. Harlow. Transport equations in turbulence. *Phys. Fluids*, 13:2634–2649, 1970.

[6] S. Fu, B. E. Launder, and D. P. Tselepidakis. *Accommodating the effects of high strain rates in modelling the pressure-strain correlation.* Dept. Mech. Eng., UMIST, March 1987. TFD/87/5.

[7] J. O. Hinze. *Turbulence.* McGraw-Hill, New York, second edition, 1975.

[8] S. Hogg and M. A. Leschziner. Computation of highly swirling confined flow with a reynolds-stress turbulence model. *AIAA J.*, 27(1), Jan, 1989.

[9] W. P. Jones and A. Pascau. Calculation of confined swirling flows with a second-moment closure. *J. Fluids Engr.*, 111:248–255, 1989.

[10] L. Le Penven, Gence J. N., and Comte-Bellot G. On the aproach to isotropy of homogeneous turbulence: effect of the partition of kinetic energy among the velocity components. In *Frontiers in Fluid Mechanics.* Springer-Verlag, 1985.

[11] R. Roback and B. V. Johnson. *Mass and momentum turbulent transport experiments with confined swirling coaxial jets*, 1983. Interim report NASA-CR-168252.

[12] T. H. Shih, J. Y. Chen, and J. L. Lumley. *Second-order modelling of boundary-free turbulent shear flows with a new model form of pressure correlation.* Sibley School of Mechanical and Aerospace Engineering, August 1985. FDA-85-07.

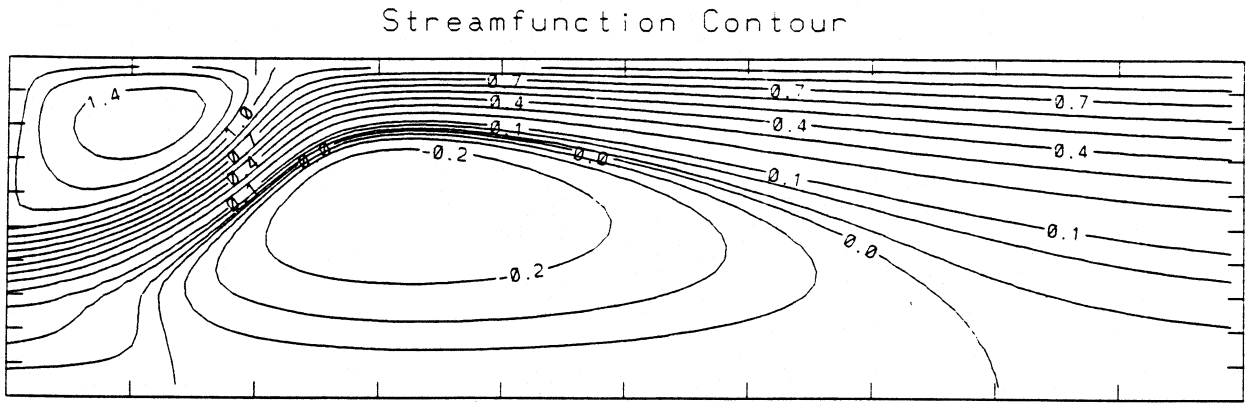

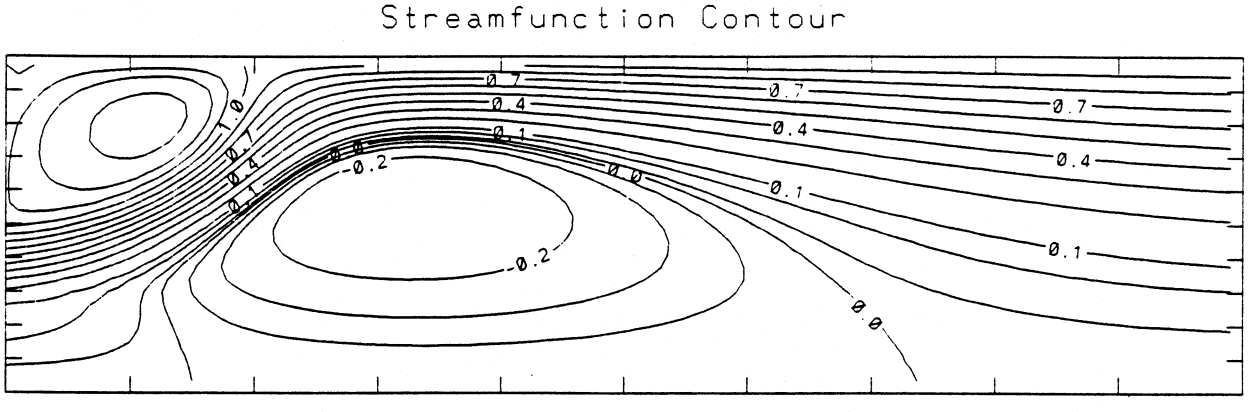

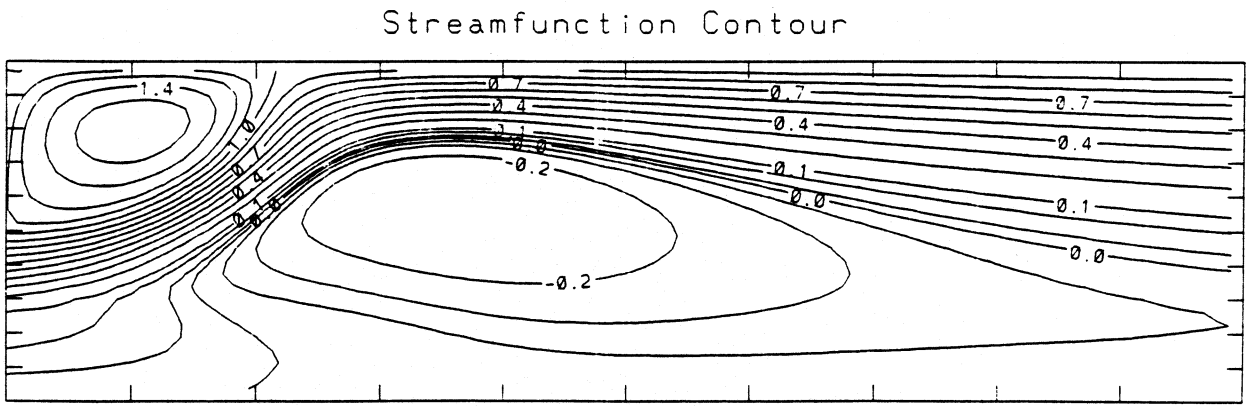

Figure 1: Contours of the streamfunctions. (a) $k - \epsilon$ model, (b) IPM, (c) GLM.

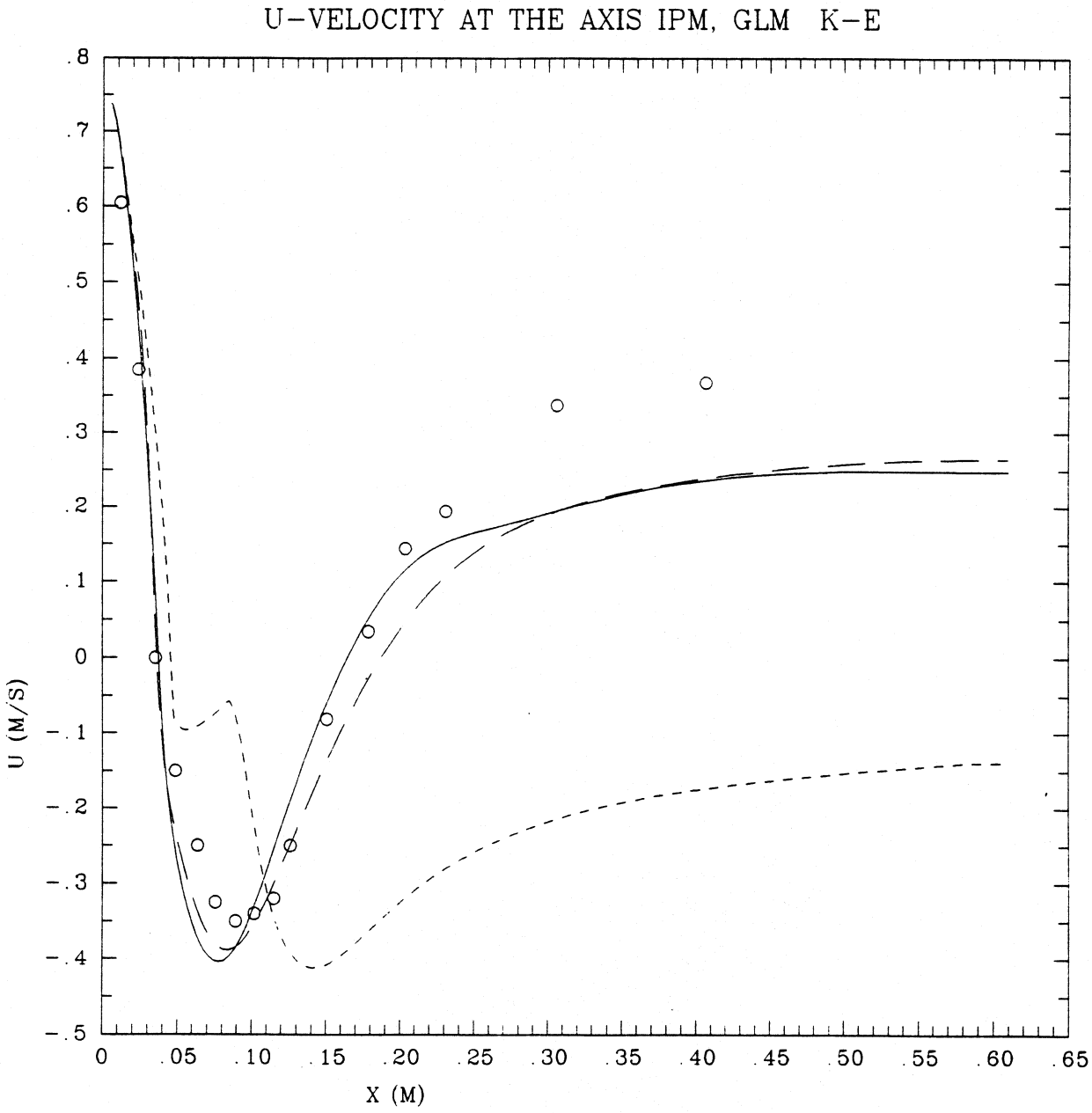

Figure 2: Axial velocity development along the aixs of symmetry; $k-\epsilon$ model, - - - ; IPM, ——; GLM, - - -.

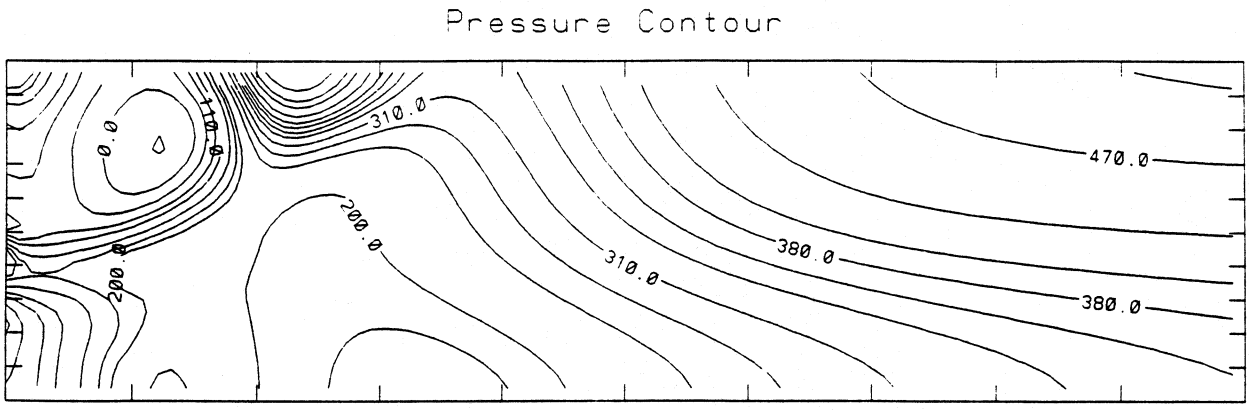

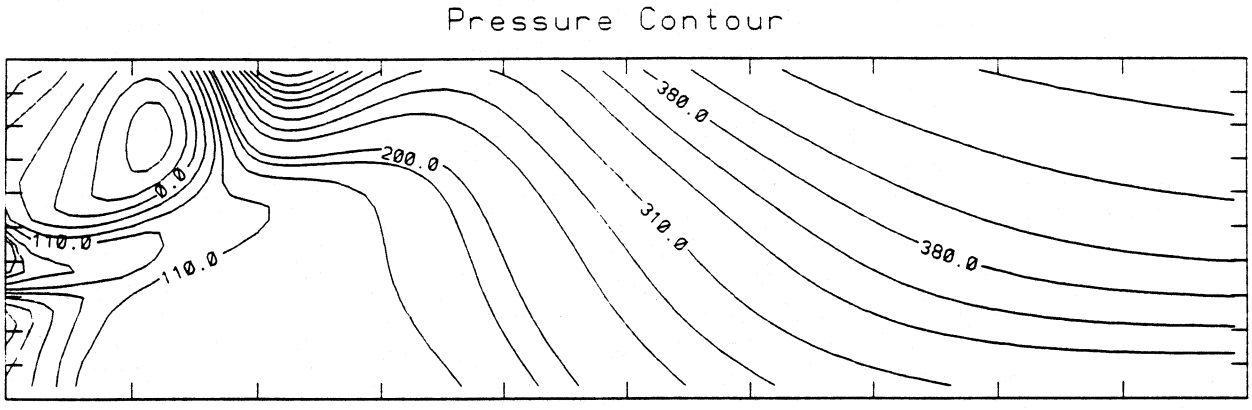

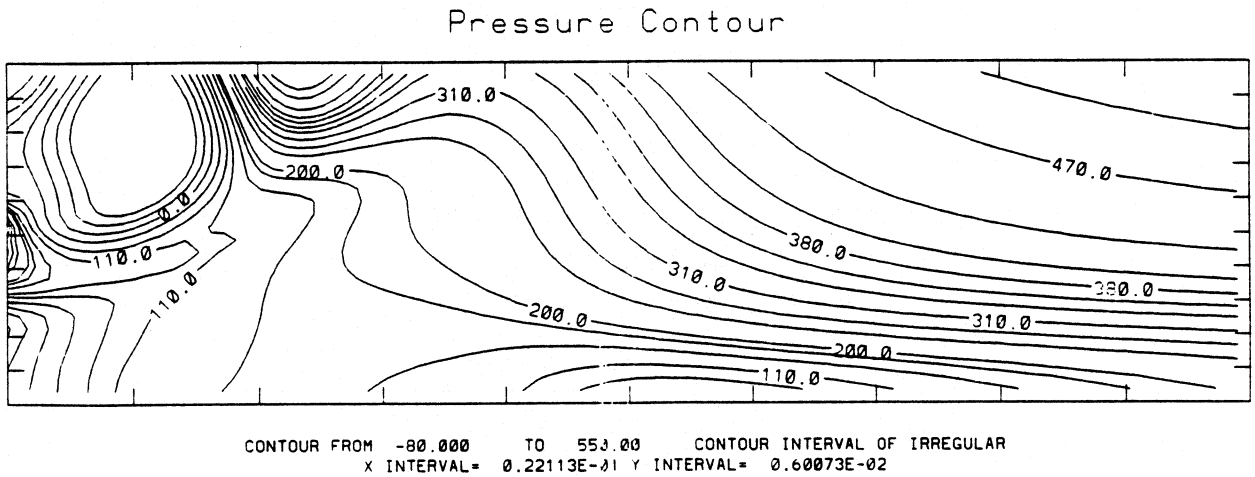

Figure 3: Contours of the pressure field. (a) $k-\epsilon$ model, (b) IPM, (c) GLM.

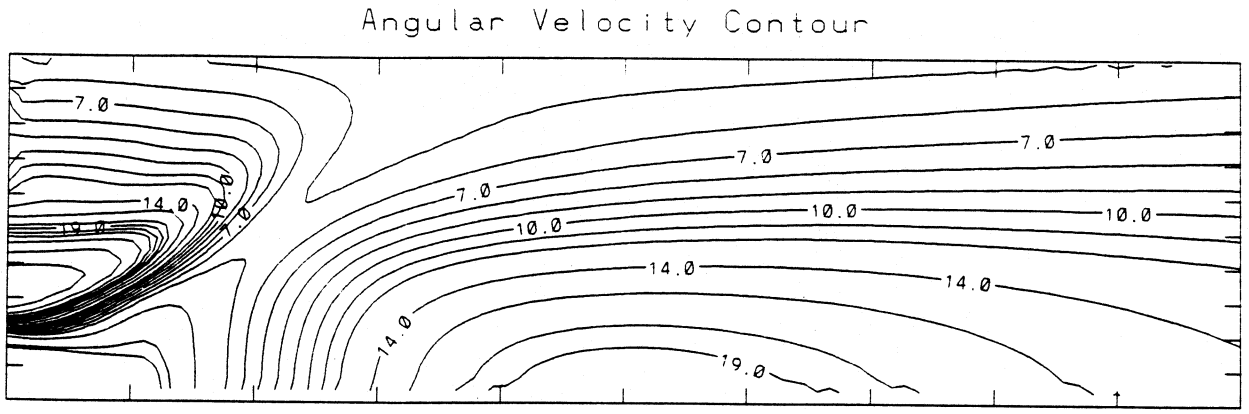

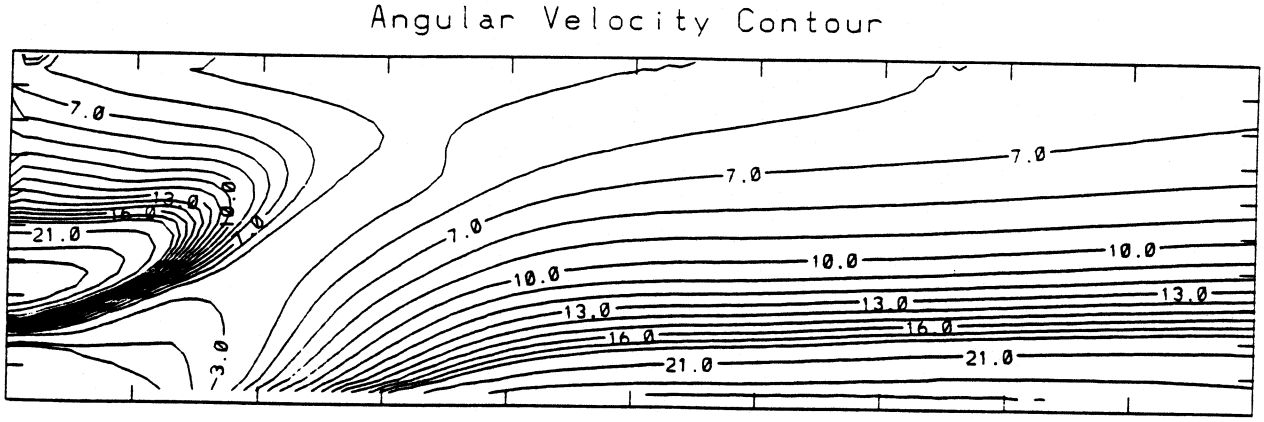

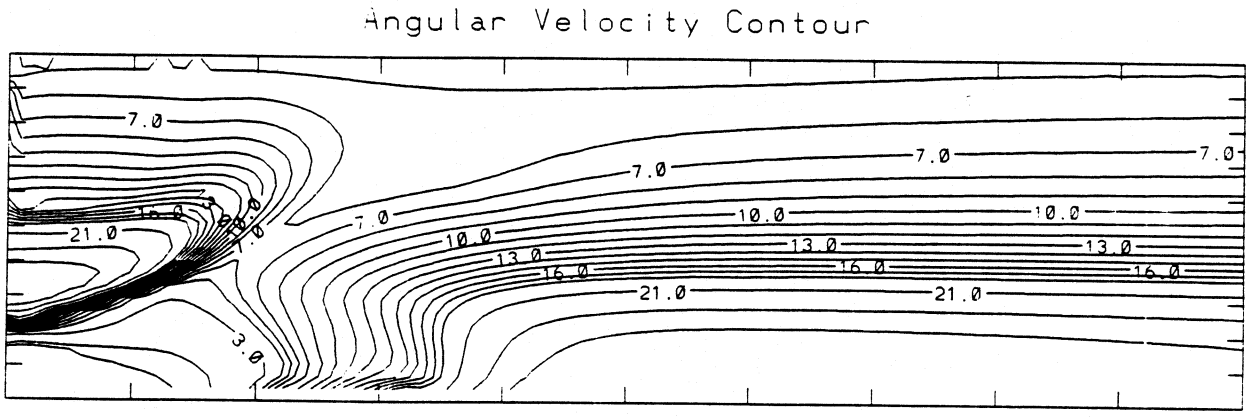

Figure 4: Contours of the angular velocity. (a) $k - \epsilon$ model, (b) IPM, (c) GLM.

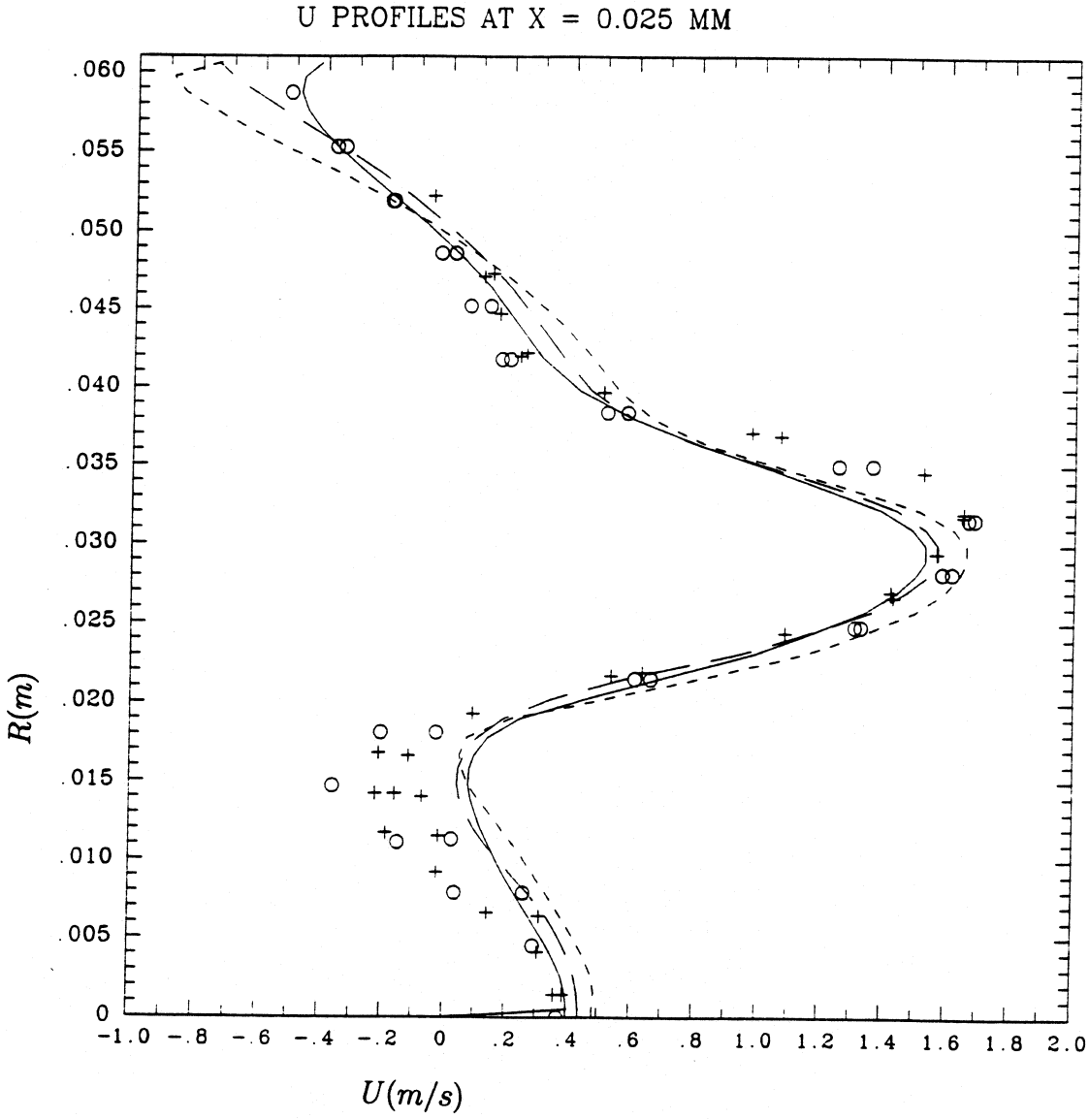

Figure 5: Axial velocity U profiles at (a) $x = 0.025m$, (b) $x = 0.051m$, (c) $x = 0.102m$, (d) $x = 0.152m$ and (e) $x = 0.203m$; $k - \epsilon$ model. - - - ; IPM, ——; GLM, - - -.

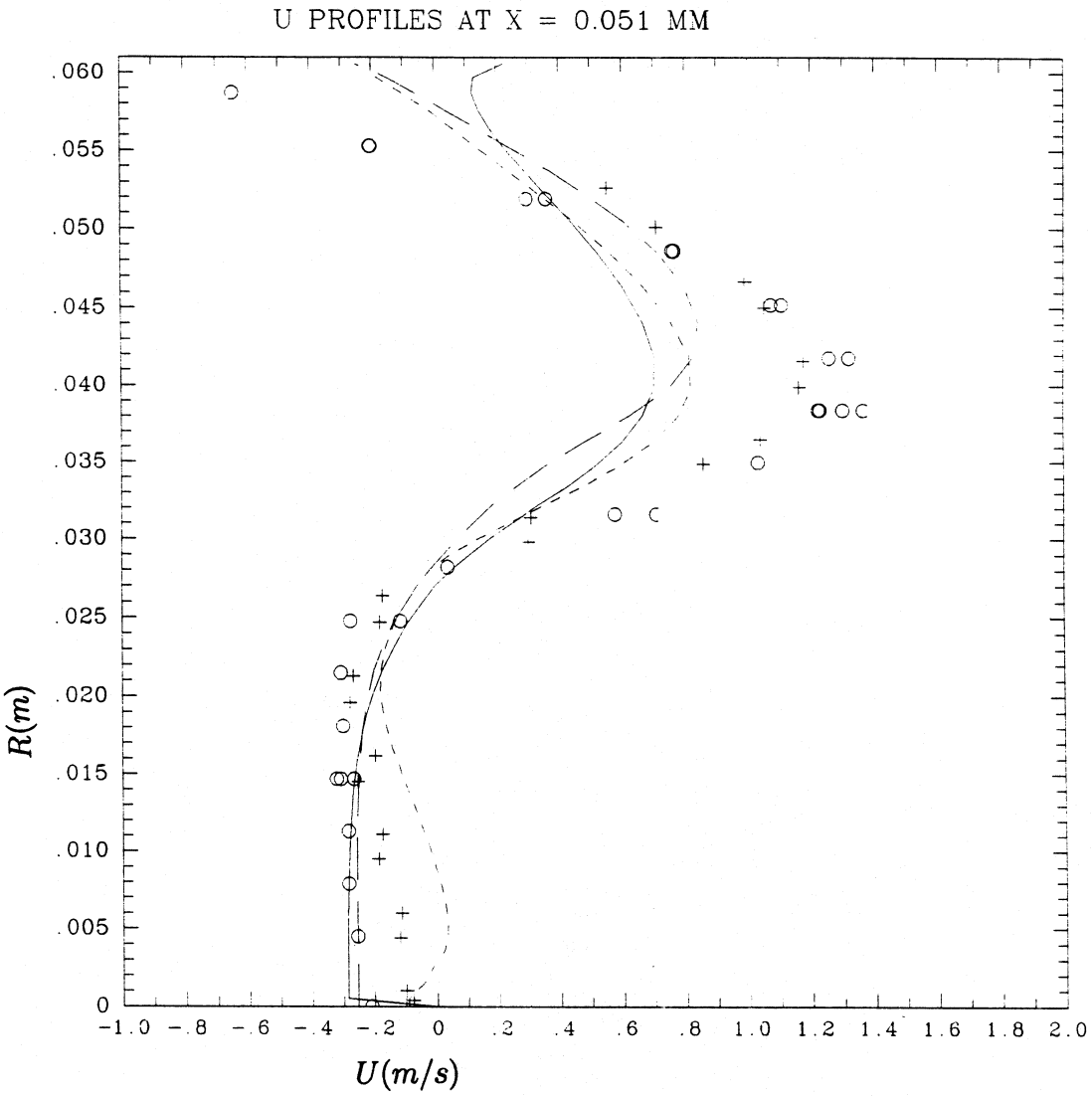
U PROFILES AT X = 0.051 MM
.060
.055
.050
.045
.040
.035
.030
.025
.020
.015
.010
.005
0
R(m)
-1.0 -.8 -.6 -.4 -.2 0 .2 .4 .6 .8 1.0 1.2 1.4 1.6 1.8 2.0
U(m/s)

Fig. 5(b)

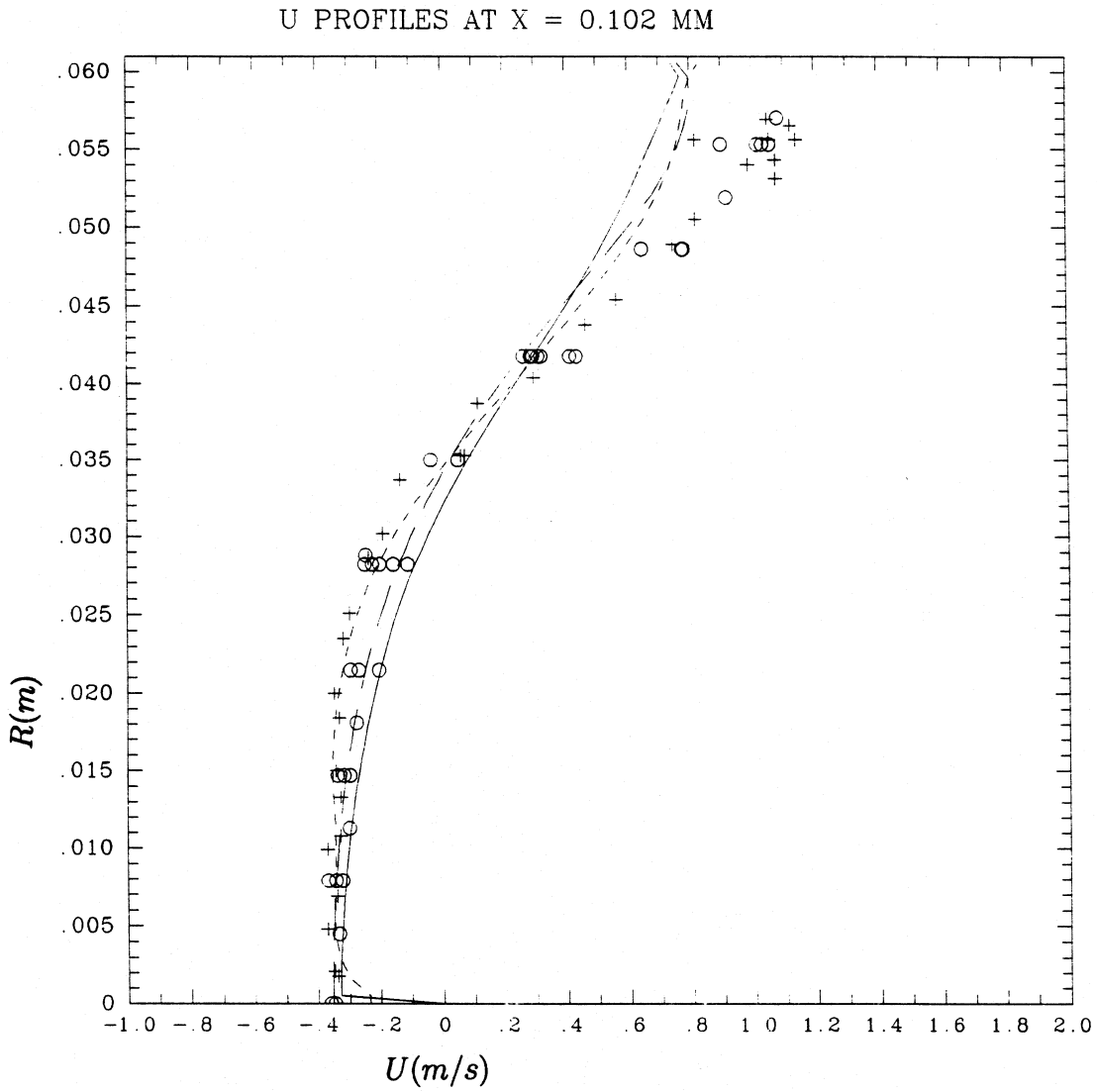
U PROFILES AT X = 0.102 MM
.060
.055
.050
.045
.040
.035
.030
.025
.020
.015
.010
.005
0
R(m)
-1.0 -.8 -.6 -.4 -.2 0 .2 .4 .6 .8 1.0 1.2 1.4 1.6 1.8 2.0
U(m/s)

Fig. 5(c)

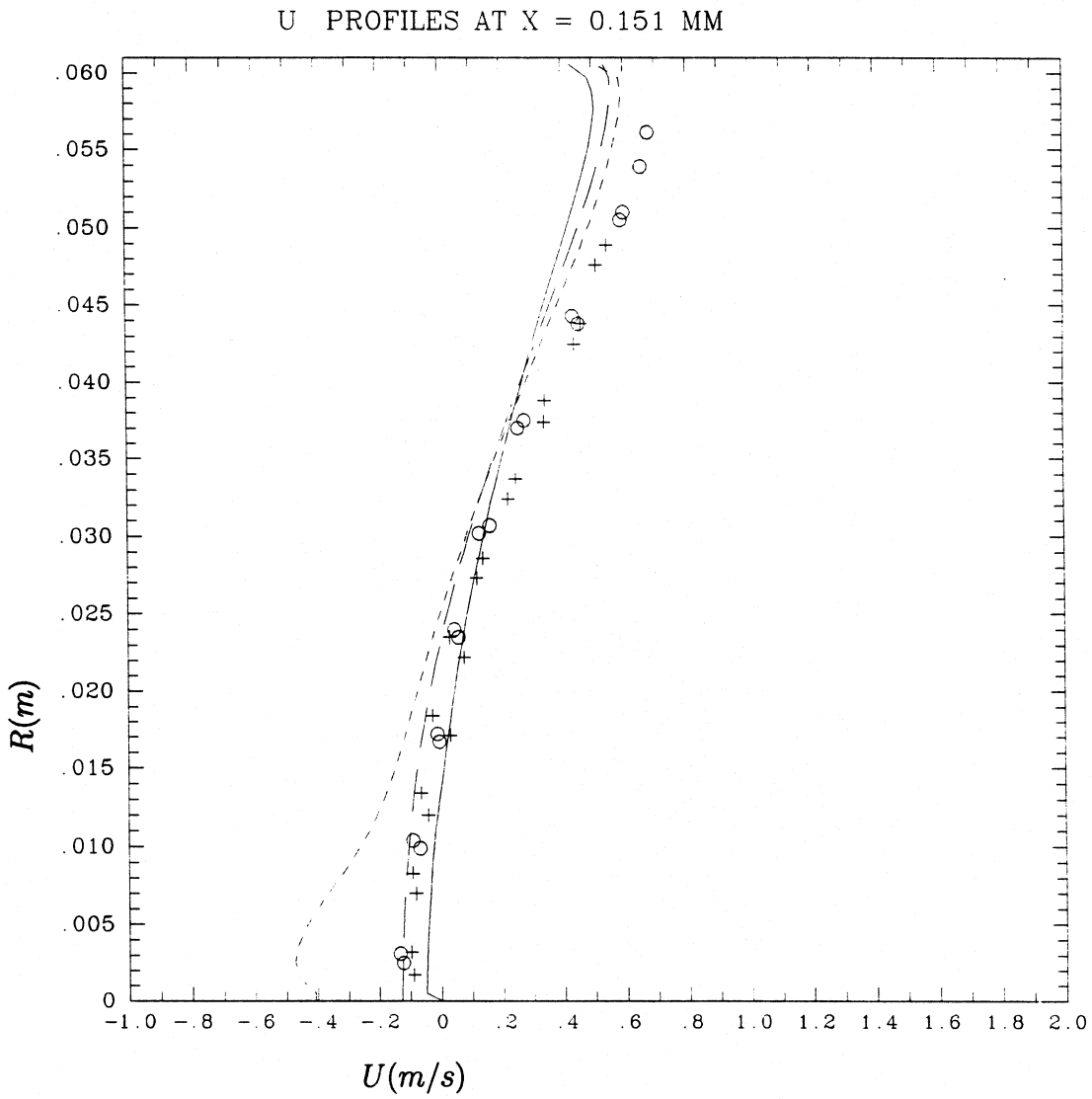
U PROFILES AT X = 0.151 MM
.060
.055
.050
.045
.040
.035
.030
.025
.020
.015
.010
.005
0
R(m)
-1.0 -.8 -.6 -.4 -.2 0 .2 .4 .6 .8 1.0 1.2 1.4 1.6 1.8 2.0
U(m/s)

Fig. 5(d)

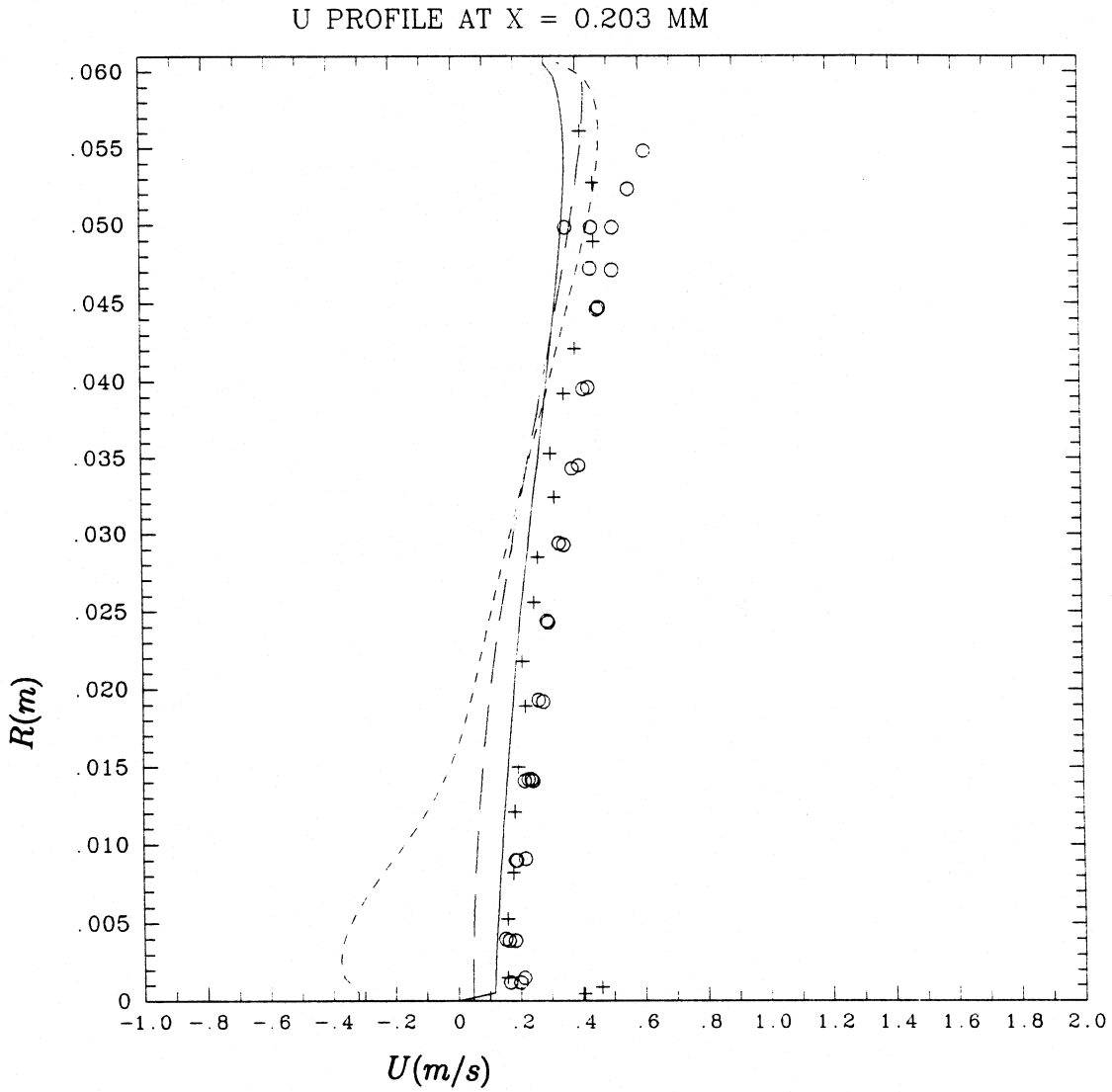
U PROFILE AT X = 0.203 MM
.060
.055
.050
.045
.040
.035
.030
.025
.020
.015
.010
.005
0
R(m)
-1.0 -.8 -.6 -.4 -.2 0 .2 .4 .6 .8 1.0 1.2 1.4 1.6 1.8 2.0
U(m/s)

Fig. 5(e)

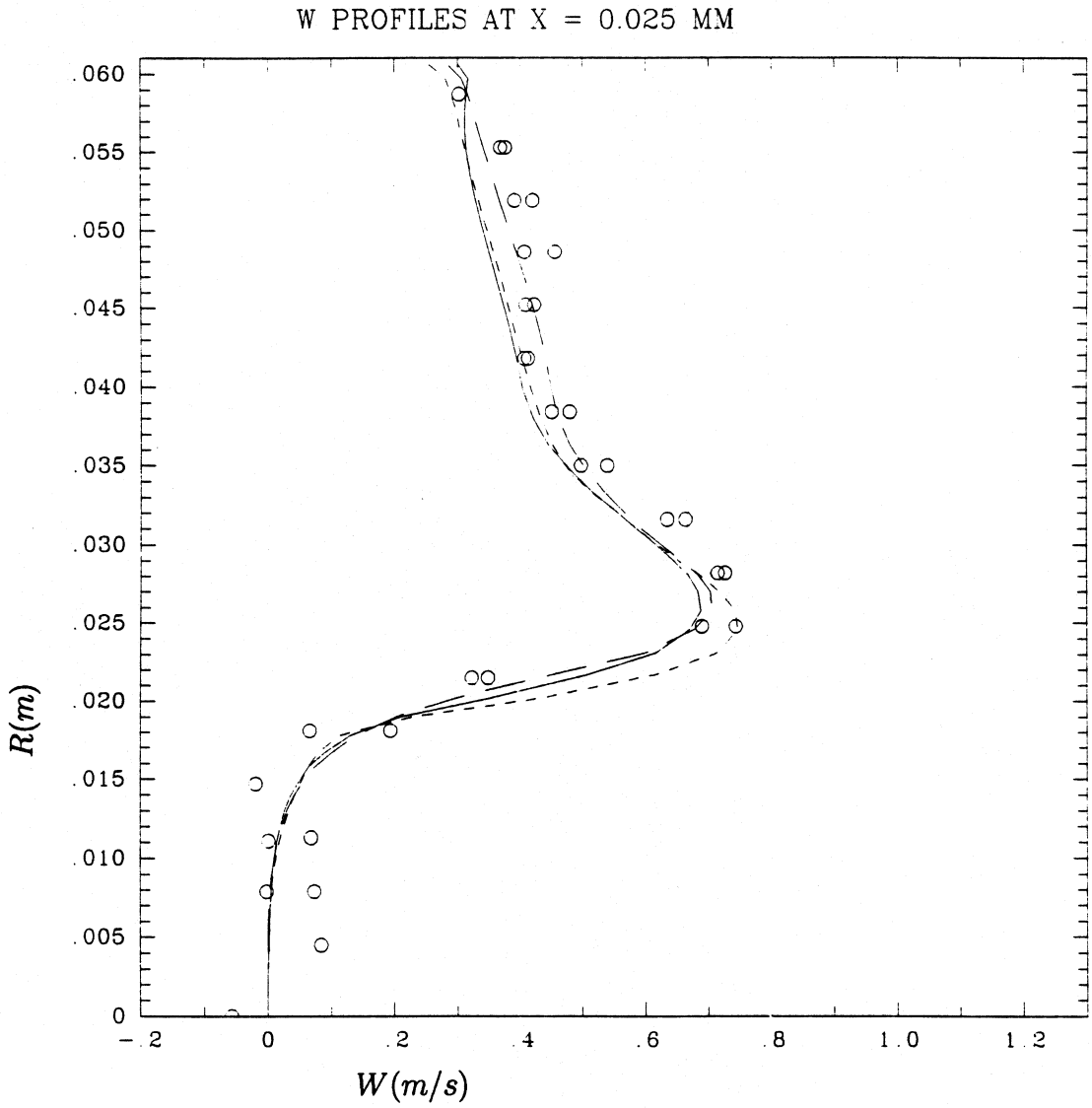

Figure 6: Swirl velocity W profiles at (a) $x = 0.025m$, (b) $x = 0.051m$, (c) $x = 0.102m$, (d) $x = 0.152m$ and (e) $x = 0.203m$; $k - \epsilon$ model, - - - ; IPM, ——; GLM, - - -.

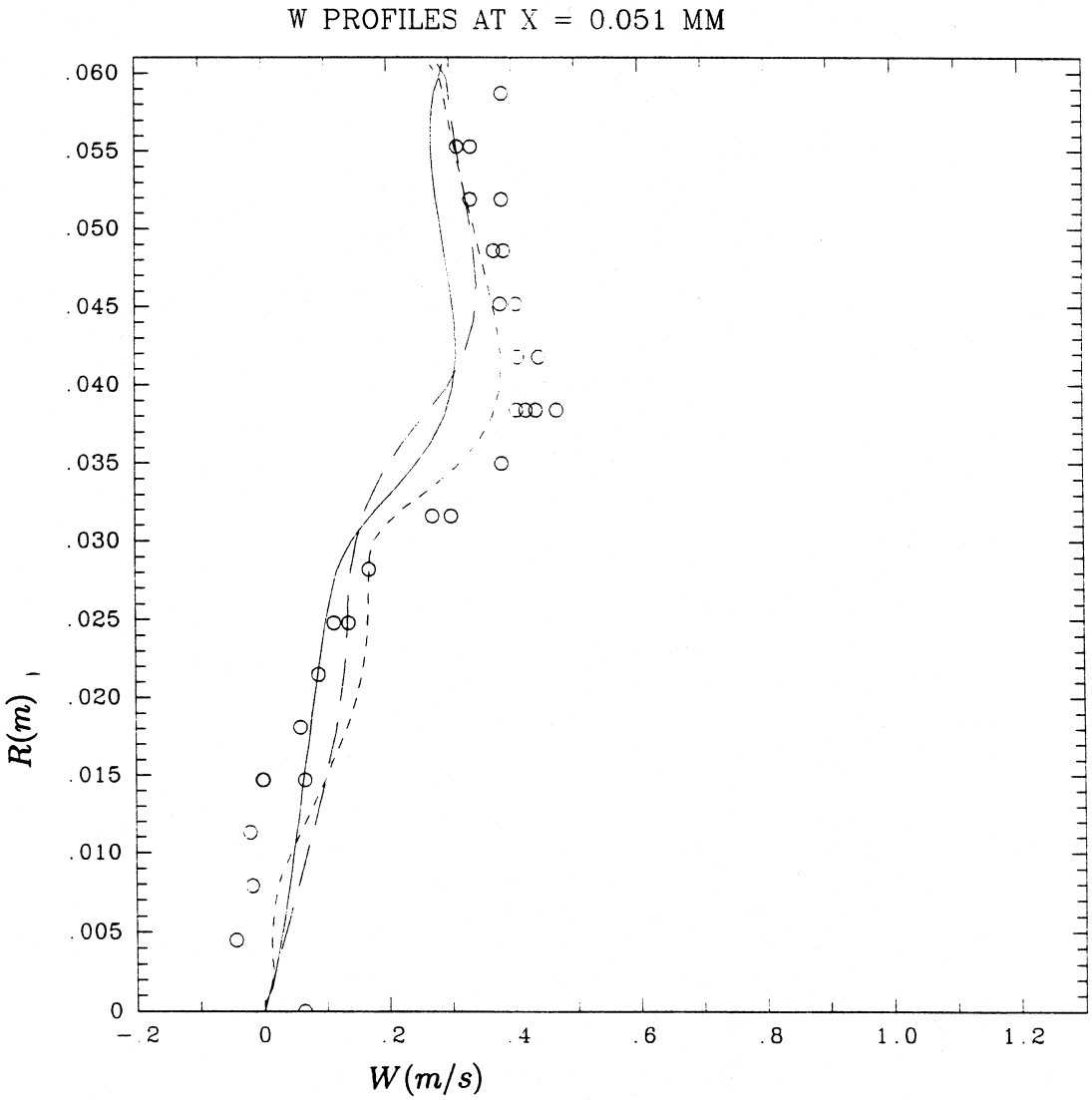
W PROFILES AT X = 0.051 MM
.060
.055
.050
.045
.040
.035
.030
.025
.020
.015
.010
.005
0
R(m)
-.2
0
.2
.4
.6
.8
1.0
1.2
W(m/s)

Fig. 6(b)

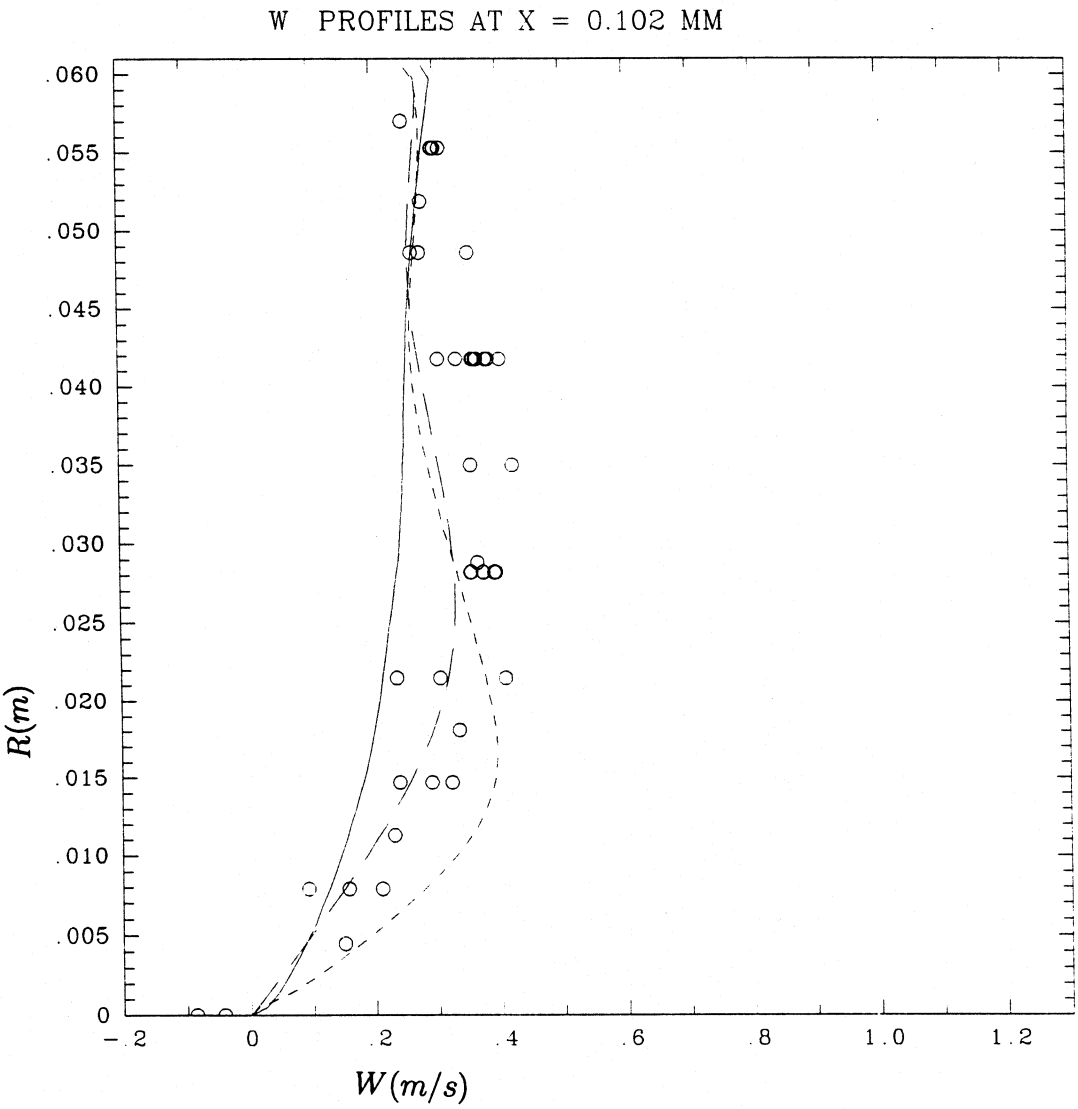
W PROFILES AT X = 0.102 MM
.060
.055
.050
.045
.040
.035
.030
.025
.020
.015
.010
.005
0
R(m)
-.2
0
.2
.4
.6
.8
1.0
1.2
W(m/s)

Fig. 6(c)

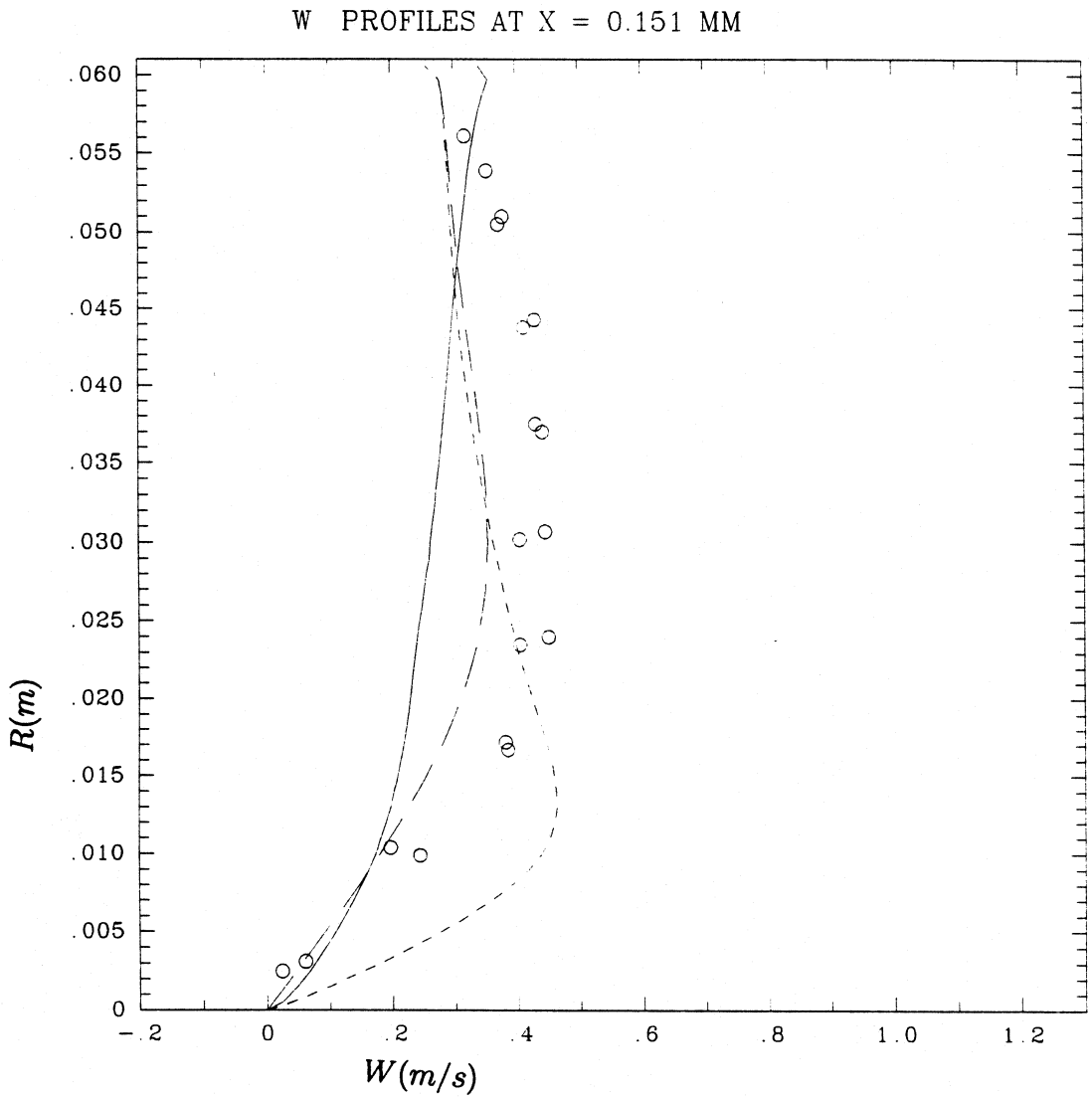
W PROFILES AT X = 0.151 MM
.060
.055
.050
.045
.040
.035
.030
.025
.020
.015
.010
.005
0
R(m)
-.2
0
.2
.4
.6
.8
1.0
1.2
W(m/s)

Fig. 6(d)

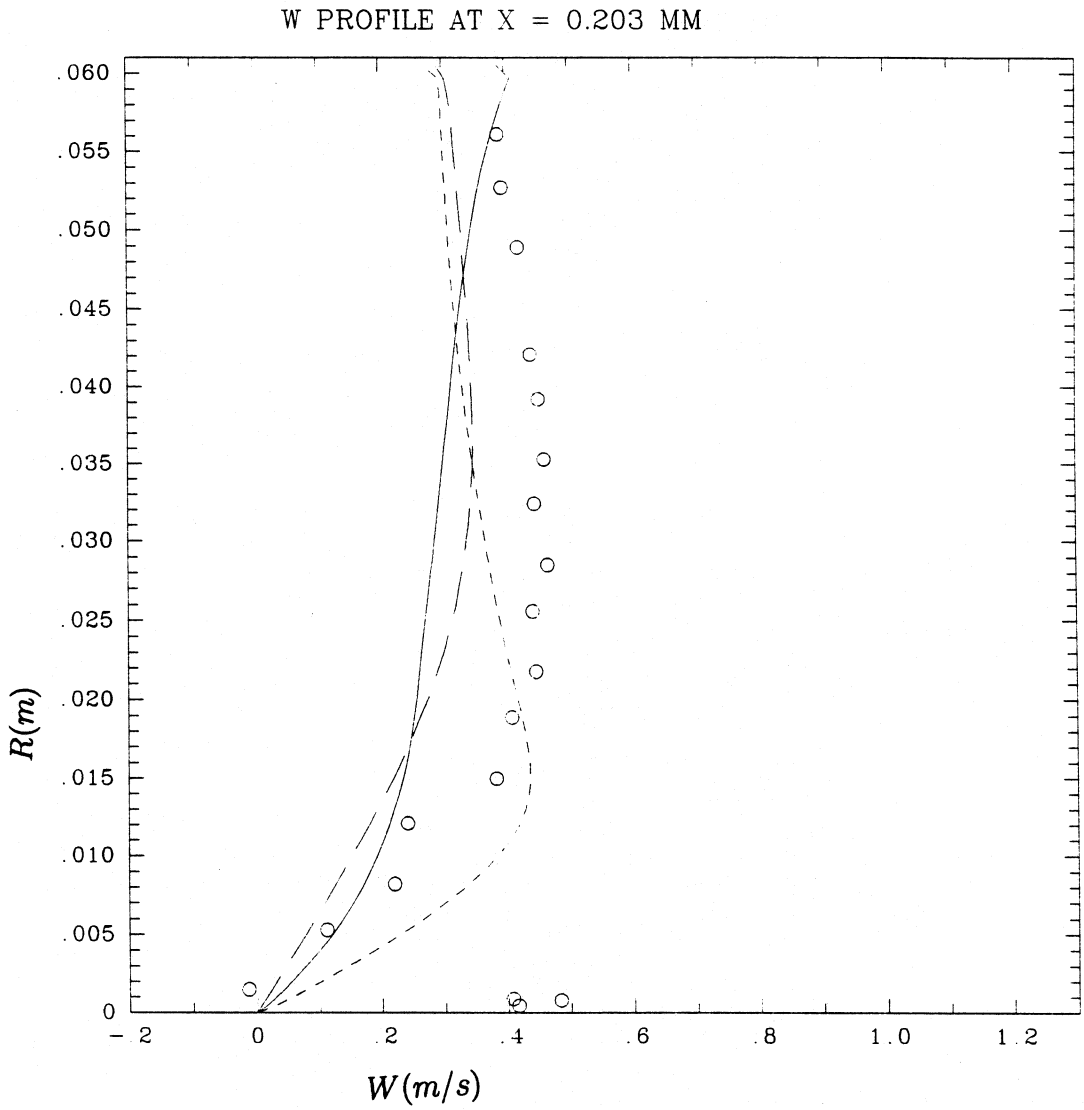
W PROFILE AT X = 0.203 MM
.060
.055
.050
.045
.040
.035
.030
.025
.020
.015
.010
.005
0
R(m)
-.2
0
.2
.4
.6
.8
1.0
1.2
W(m/s)

Fig. 6(e)

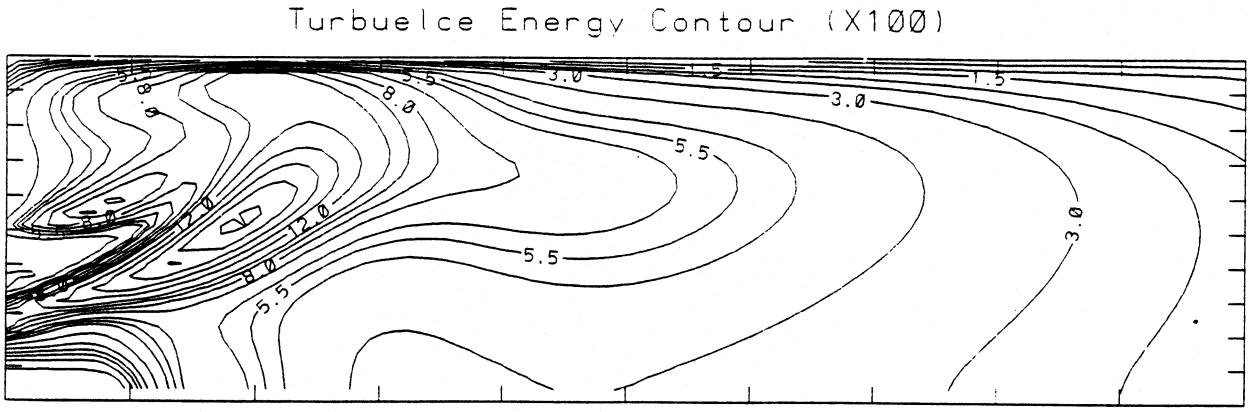

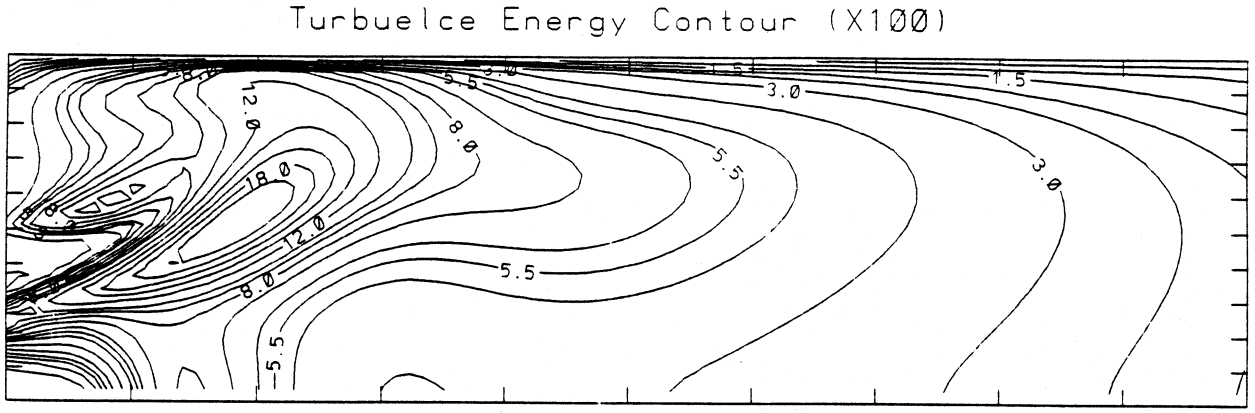

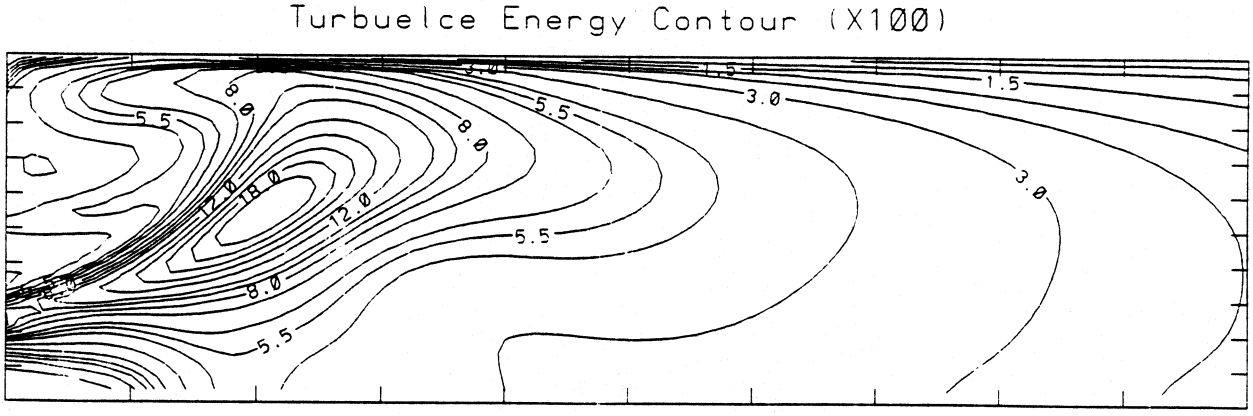

Figure 7: Contours of the turbulence kinetic energy. (a) $k - \epsilon$ model, (b) IPM, (c) GLM.

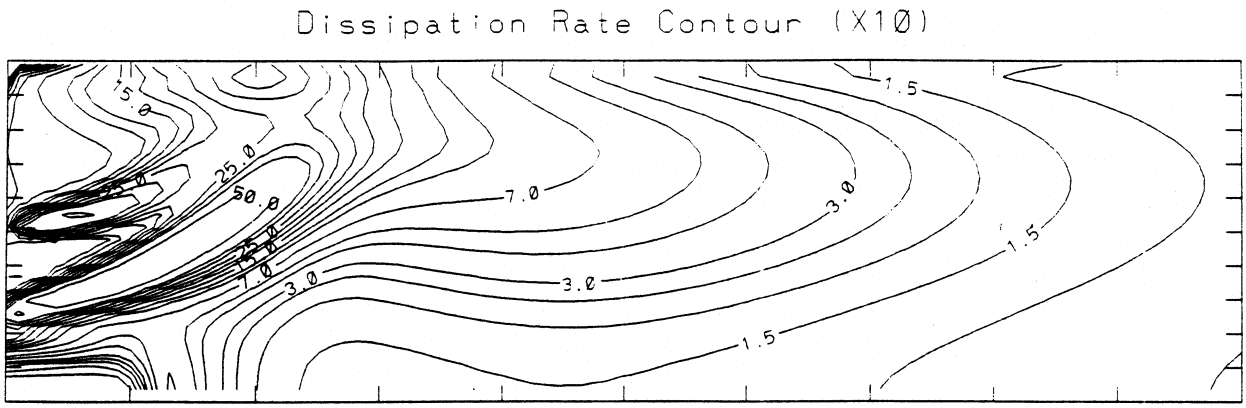

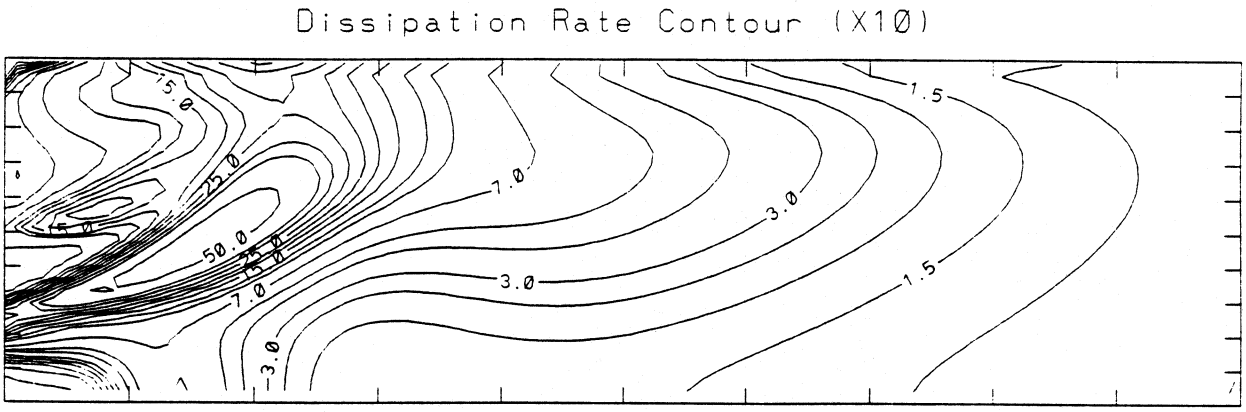

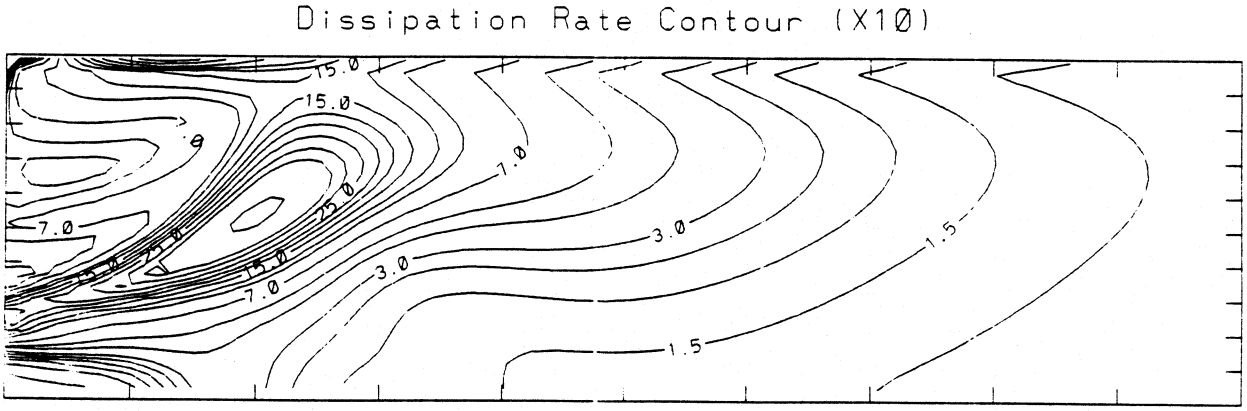

Figure 8: Contours of the dissipation rate. (a) $k - \epsilon$ model, (b) IPM, (c) GLM.

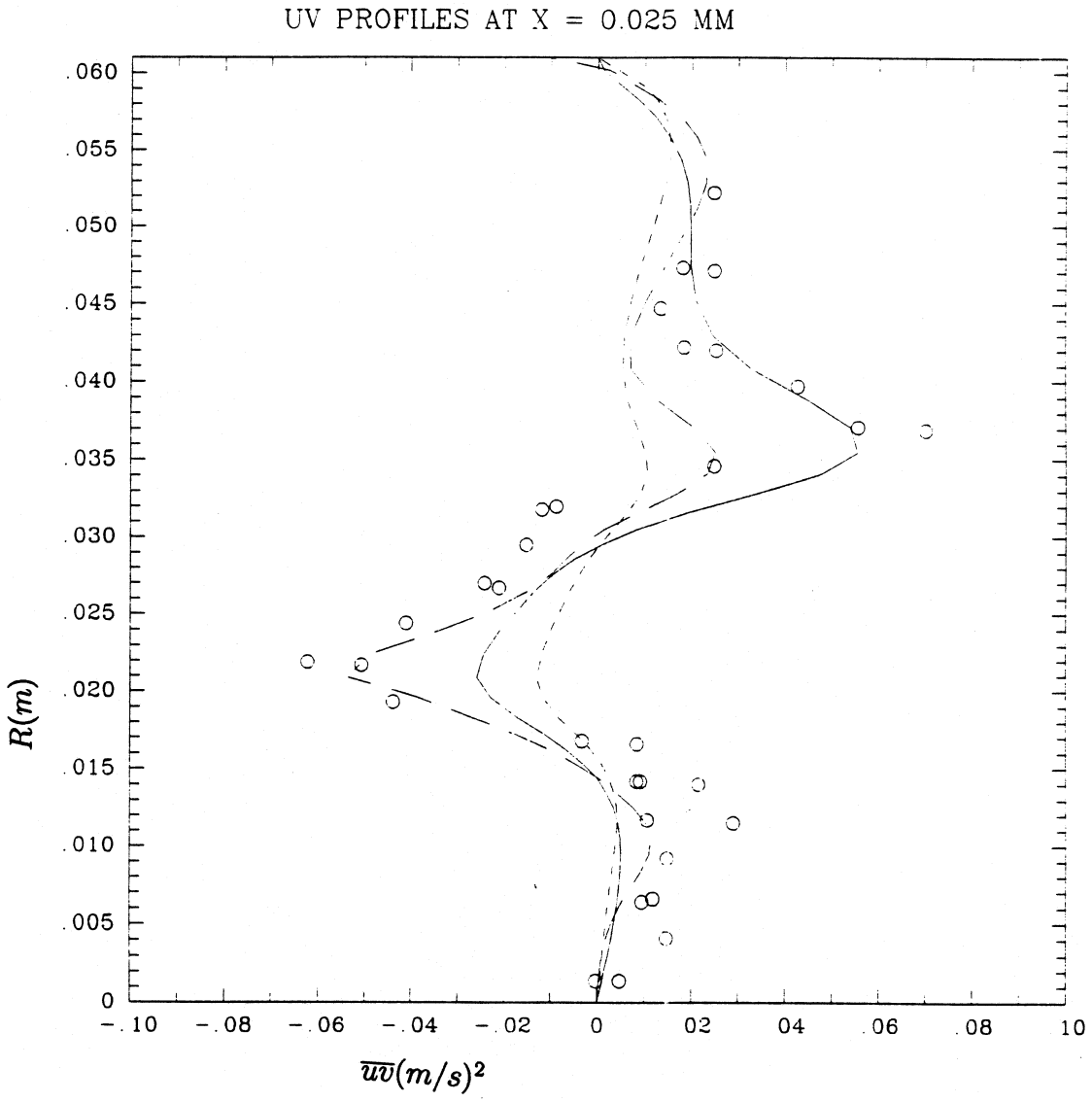

Figure 9: Shear stress $\overline{uv}$ profiles at (a) $x = 0.025m$, (b) $x = 0.051m$, (c) $x = 0.102m$, (d) $x = 0.152m$ and (e) $x = 0.203m$; $k - \epsilon$ model, - - - ; IPM, ——; GLM, - - -.

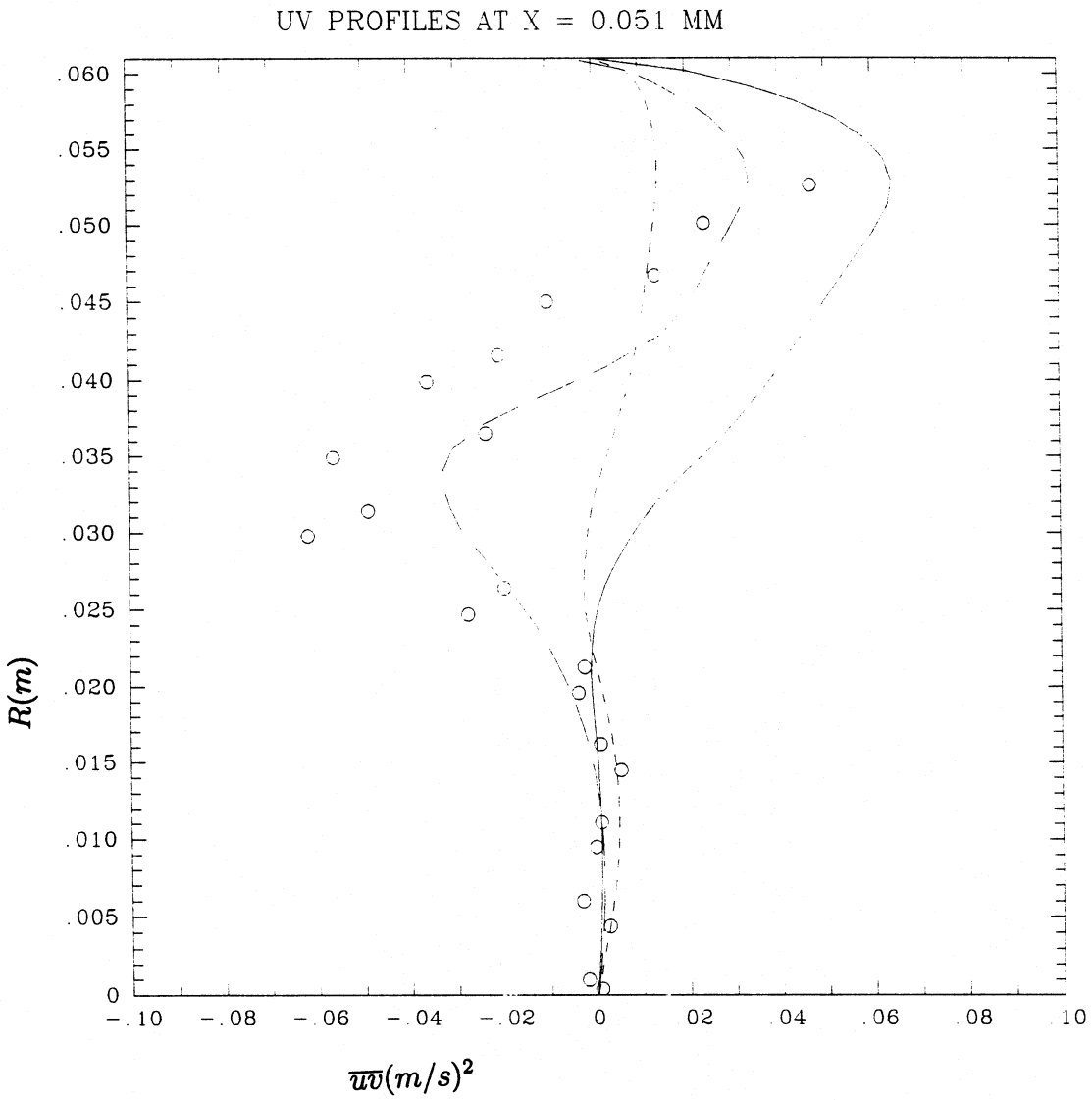
UV PROFILES AT X = 0.051 MM
.060
.055
.050
.045
.040
.035
.030
.025
.020
.015
.010
.005
0
R(m)
-.10
-.08
-.06
-.04
-.02
0
02
.04
.06
.08
.10
$\overline{uv}(m/s)^2$

Fig. 9(b)

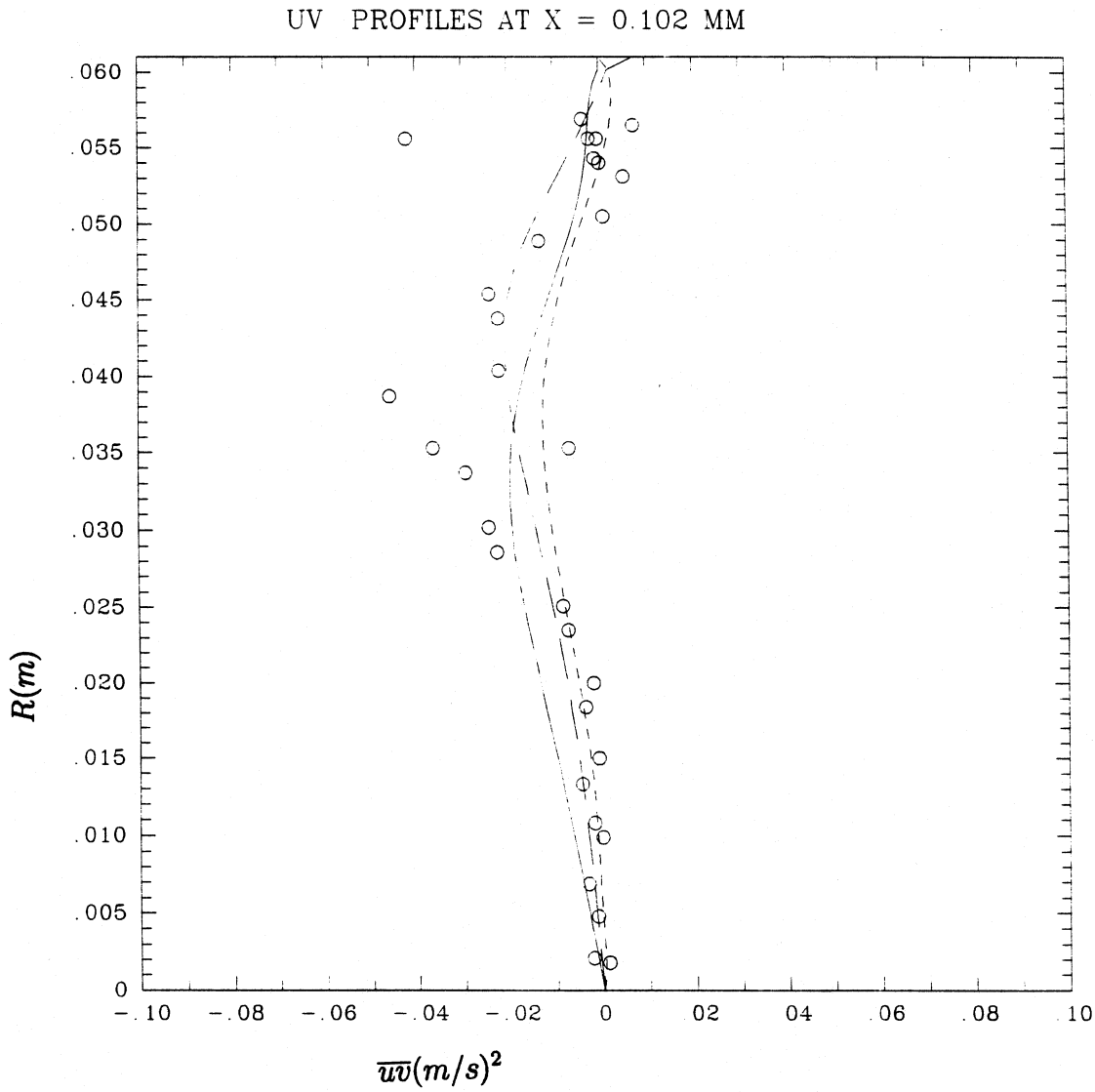
UV PROFILES AT X = 0.102 MM
.060
.055
.050
.045
.040
.035
.030
.025
.020
.015
.010
.005
0
R(m)
-.10
-.08
-.06
-.04
-.02
0
02
04
06
08
10
$\overline{uv}(m/s)^2$

Fig. 9(c)

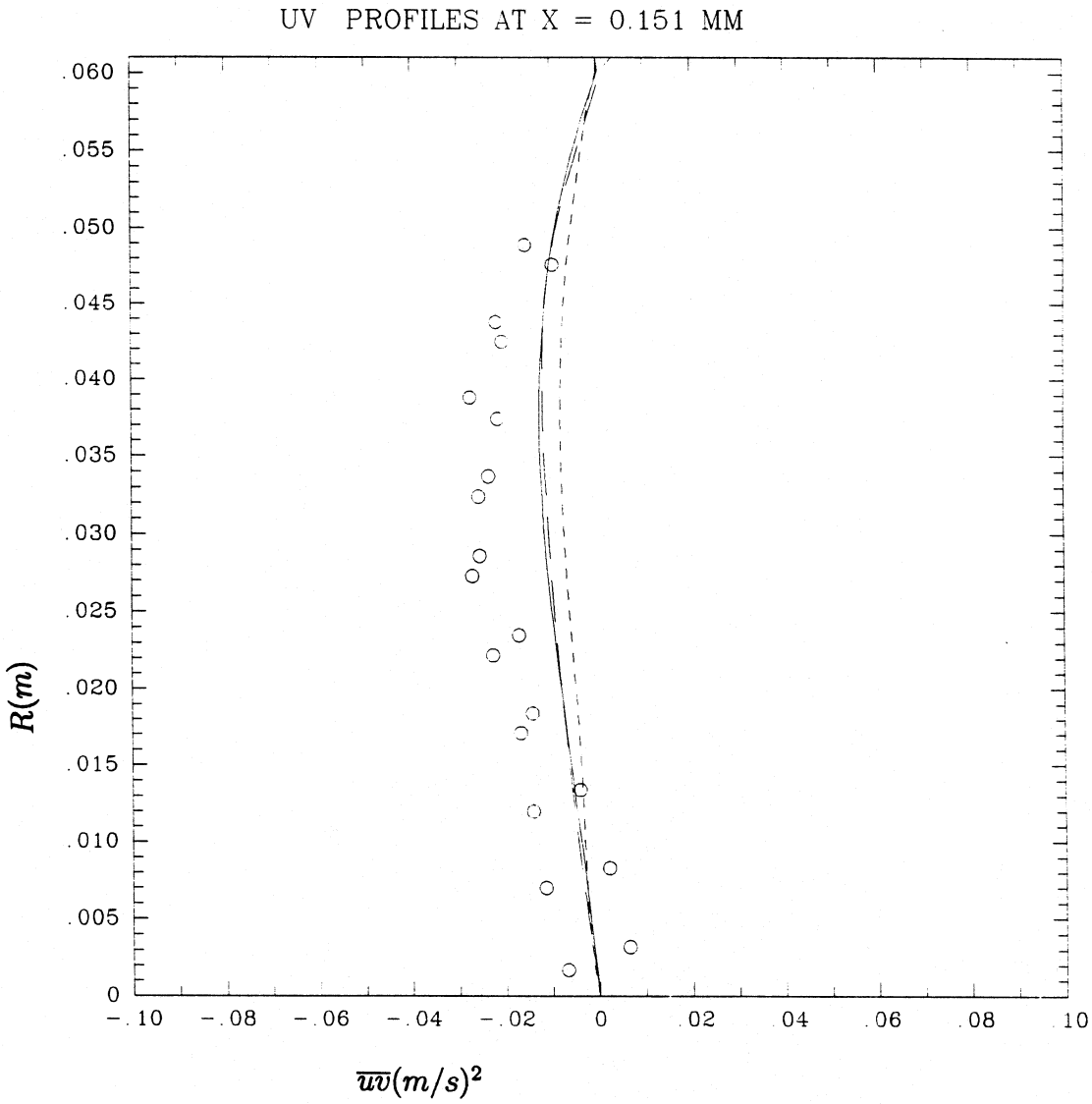
UV PROFILES AT X = 0.151 MM
.060
.055
.050
.045
.040
.035
.030
.025
.020
.015
.010
.005
0
R(m)
−.10
−.08
−.06
−.04
−.02
0
.02
.04
.06
.08
.10
$\overline{uv}(m/s)^2$

Fig. 9(d)

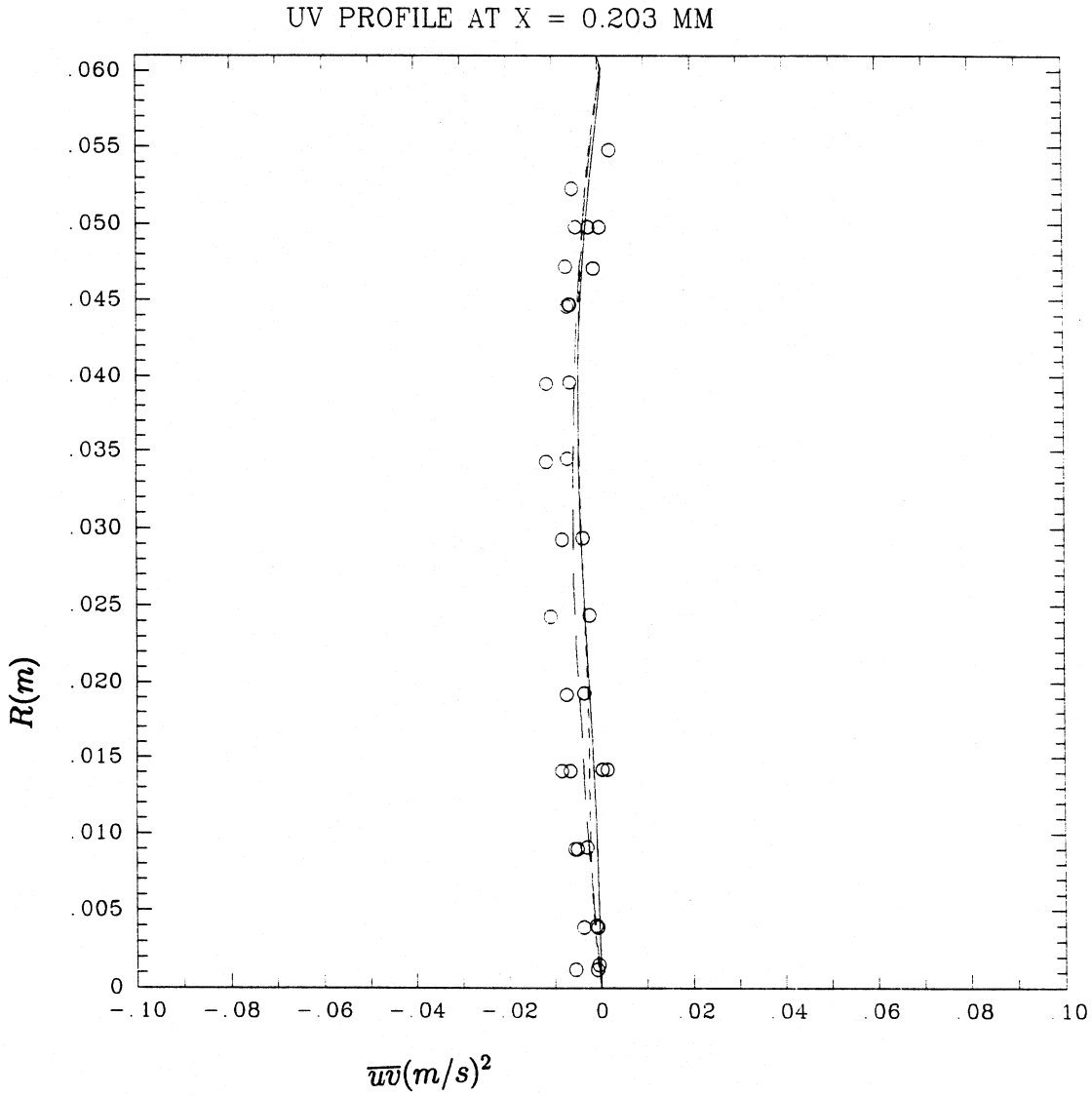
UV PROFILE AT X = 0.203 MM
.060
.055
.050
.045
.040
.035
.030
.025
.020
.015
.010
.005
0
R(m)
-.10
-.08
-.06
-.04
-.02
0
.02
.04
.06
.08
.10
$\overline{uv}(m/s)^2$

Fig. 9(e)

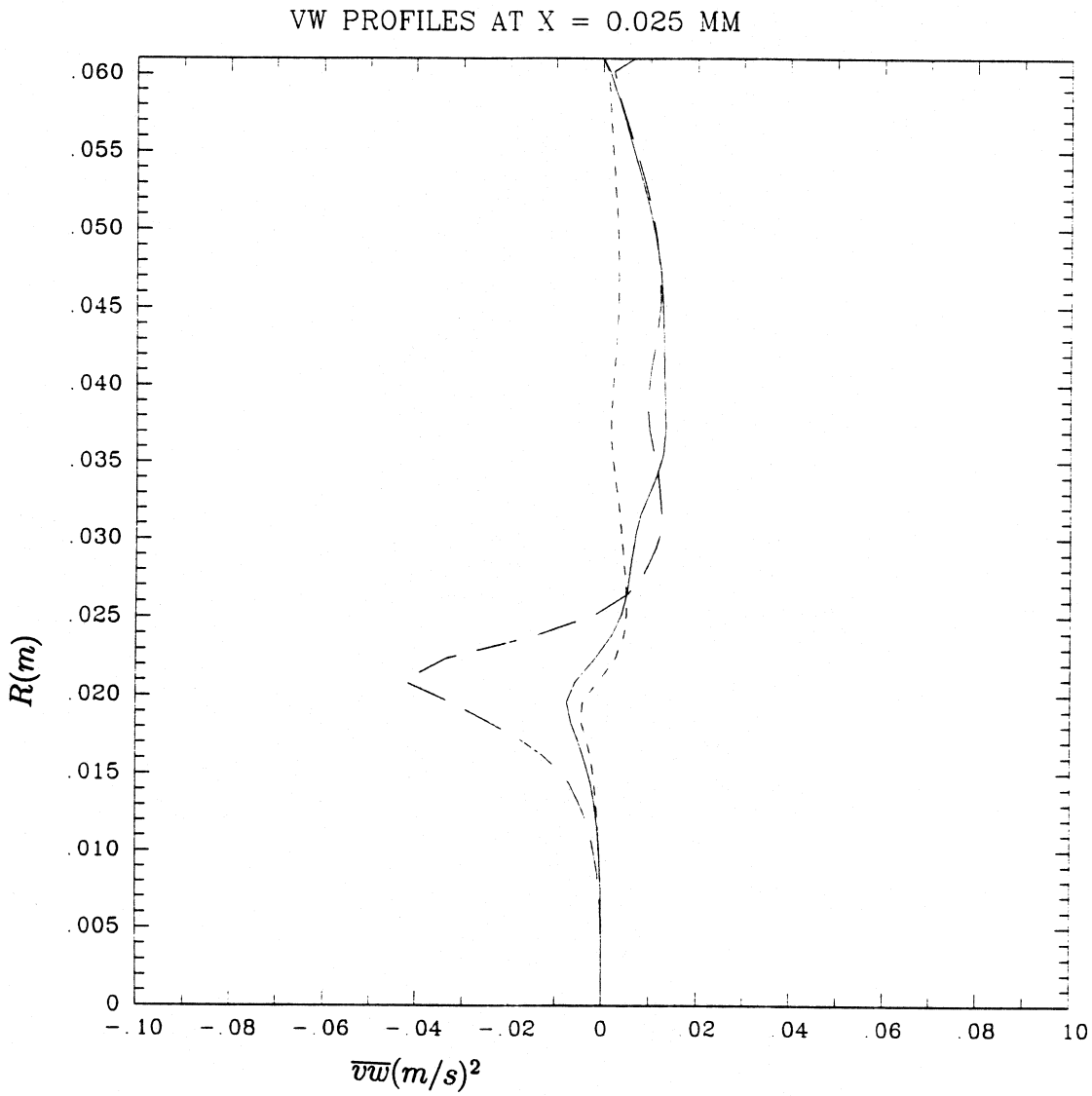

Figure 10: Shear stress $\overline{vw}$ profiles at (a) $x = 0.025m$, (b) $x = 0.051m$, (c) $x = 0.102m$, (d) $x = 0.152m$ and (e) $x = 0.203m$; $k - \epsilon$ model, - - - ; IPM, ——; GLM, - - -.

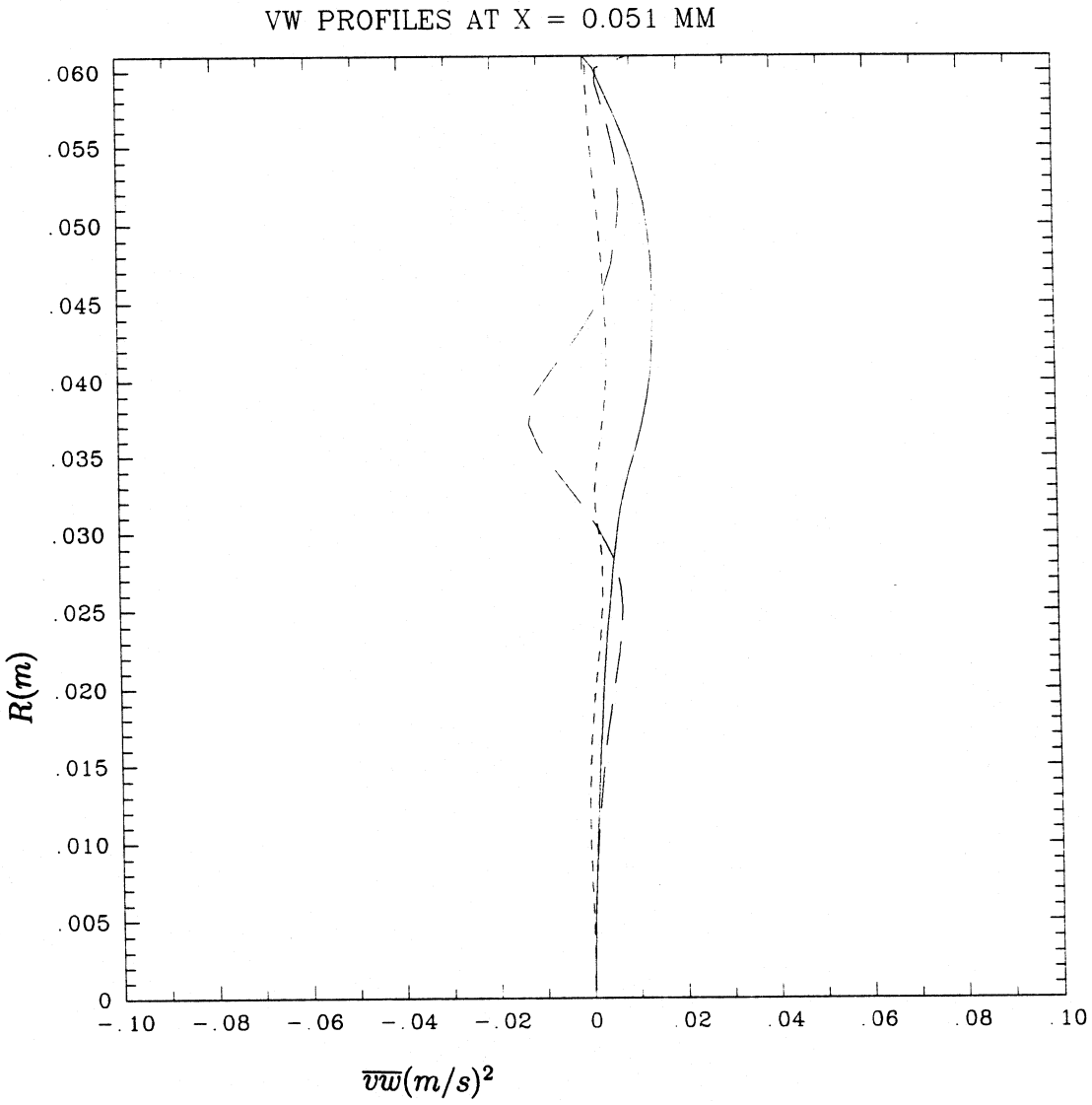
VW PROFILES AT X = 0.051 MM
.060
.055
.050
.045
.040
.035
.030
.025
.020
.015
.010
.005
0
R(m)
−.10
−.08
−.06
−.04
−.02
0
.02
.04
.06
.08
.10
$\overline{vw}(m/s)^2$

Fig. 10(b)

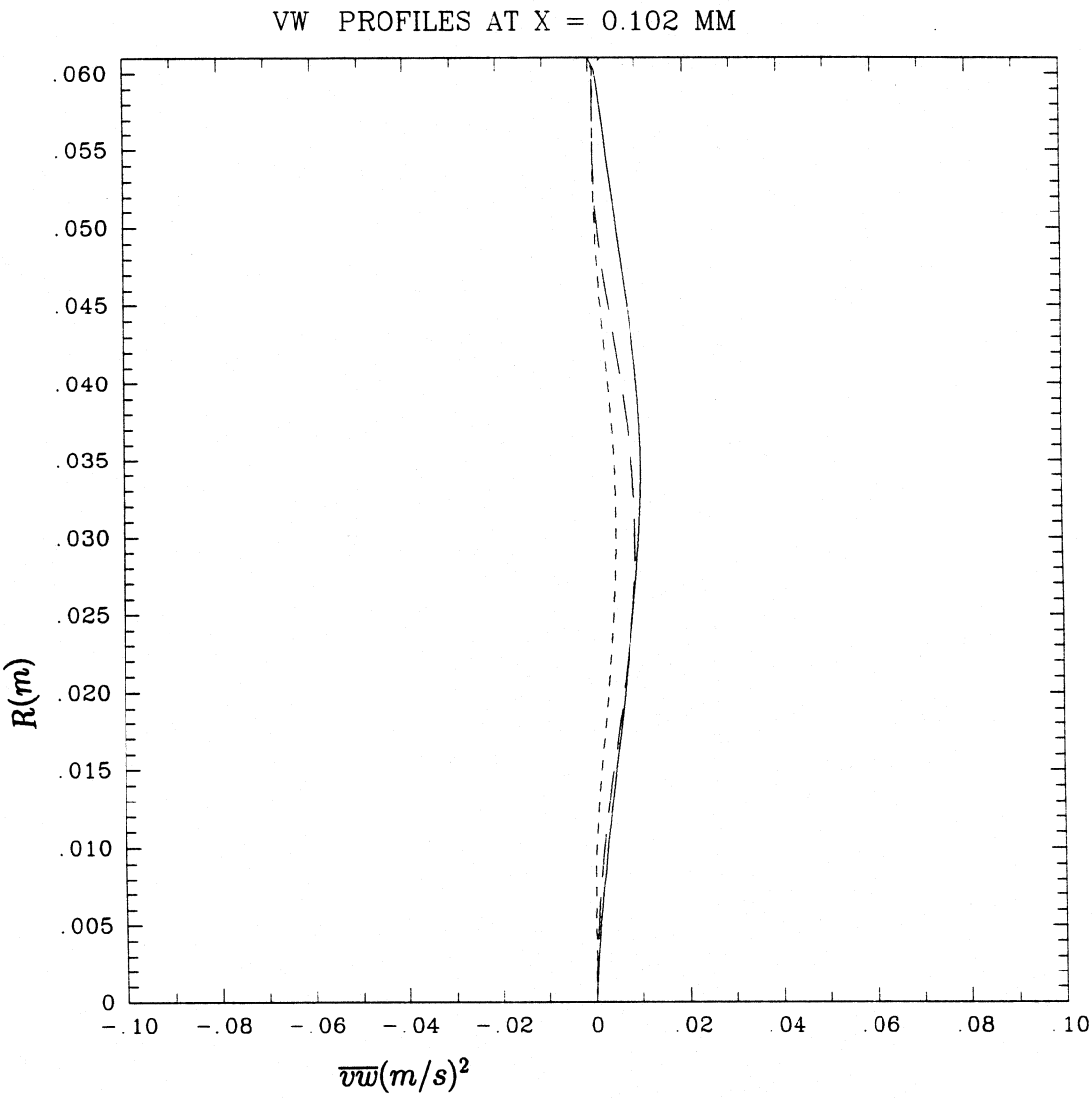
VW PROFILES AT X = 0.102 MM
.060
.055
.050
.045
.040
.035
.030
.025
.020
.015
.010
.005
0
R(m)
−.10
−.08
−.06
−.04
−.02
0
.02
.04
.06
.08
.10
$\overline{vw}(m/s)^2$

Fig. 10(c)

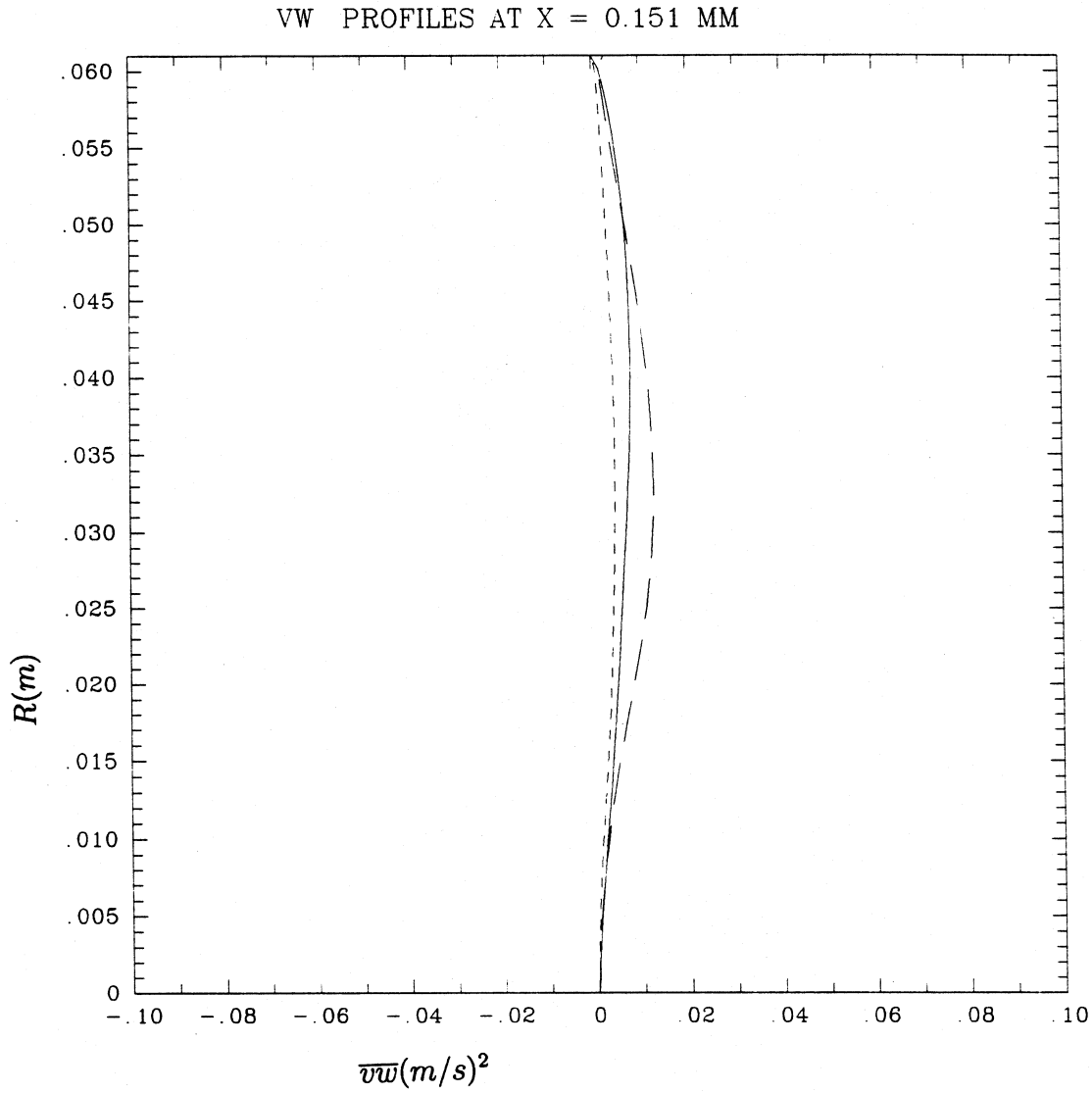
VW PROFILES AT X = 0.151 MM
.060
.055
.050
.045
.040
.035
.030
.025
.020
.015
.010
.005
0
R(m)
-.10
-.08
-.06
-.04
-.02
0
.02
.04
.06
.08
.10
$\overline{vw}(m/s)^2$

Fig. 10(d)

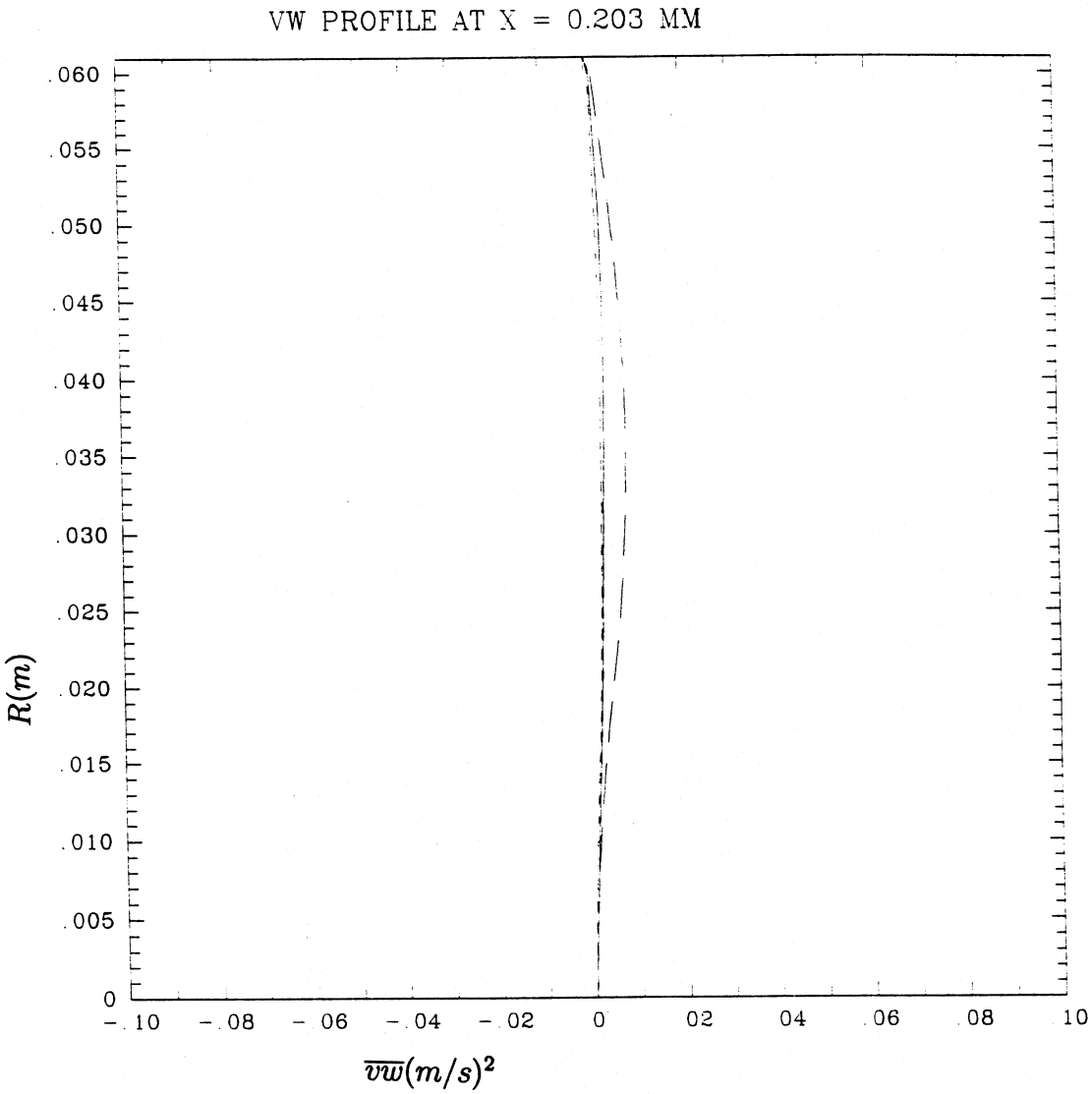
VW PROFILE AT X = 0.203 MM
.060
.055
.050
.045
.040
.035
.030
.025
.020
.015
.010
.005
0
R(m)
-.10
-.08
-.06
-.04
-.02
0
02
04
06
08
10
$\overline{vw}(m/s)^2$

Fig. 10(e)

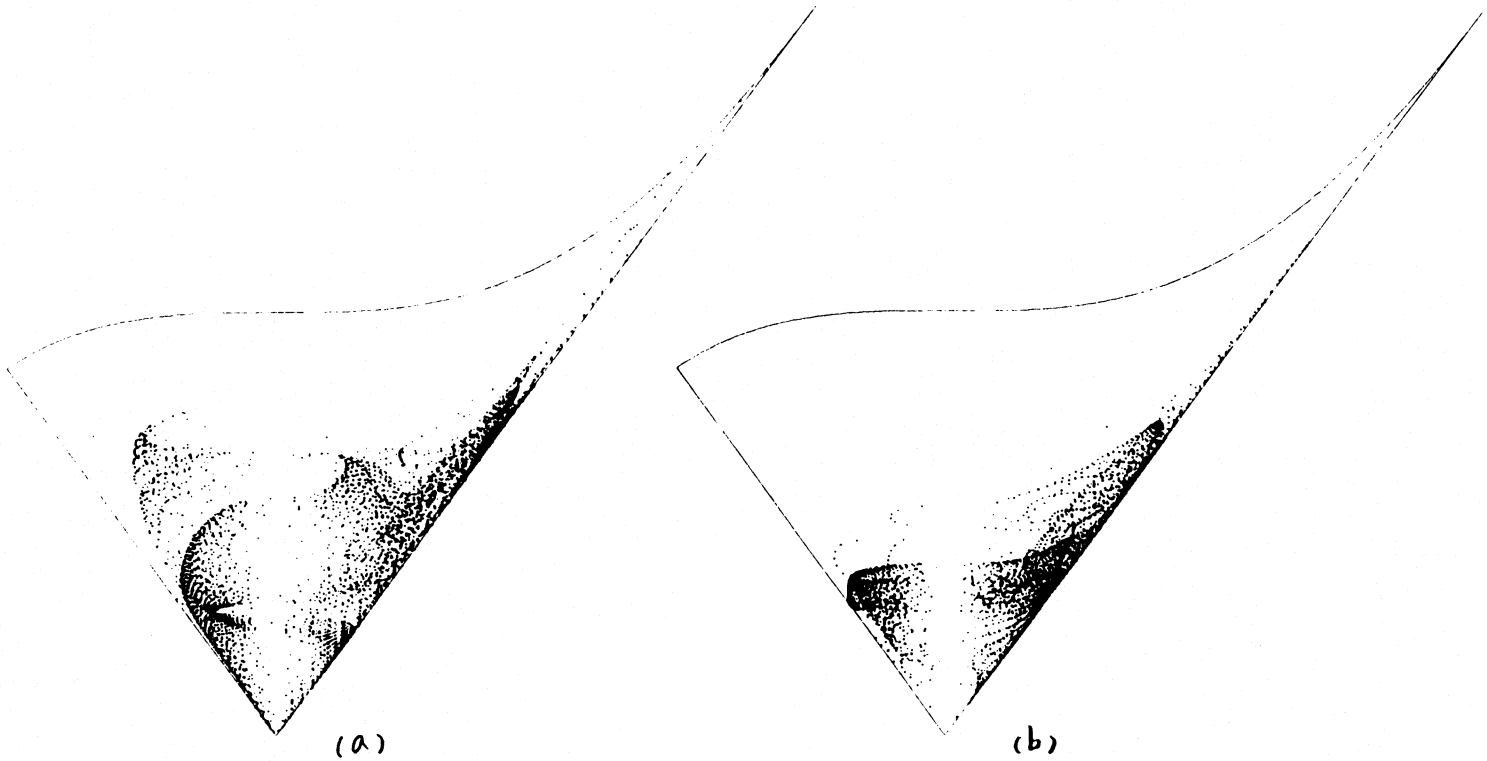

Figure 11: The anisotropy invariant maps: (a) IPM, (b) GLM.